Review Articles

Sound Out the Deep Colors: Photoacoustic Molecular Imaging at New Depths

Mucong Li[1], Nikhila Nyayapathi[2], Hailey I. Kilian[2], Jun Xia[2], Jonathan F. Lovell[2], and Junjie Yao[1]

Abstract

Photoacoustic tomography (PAT) has become increasingly popular for molecular imaging due to its unique optical absorption contrast, high spatial resolution, deep imaging depth, and high imaging speed. Yet, the strong optical attenuation of biological tissues has traditionally prevented PAT from penetrating more than a few centimeters and limited its application for studying deeply seated targets. A variety of PAT technologies have been developed to extend the imaging depth, including employing deep-penetrating microwaves and X-ray photons as excitation sources, delivering the light to the inside of the organ, reshaping the light wavefront to better focus into scattering medium, as well as improving the sensitivity of ultrasonic transducers. At the same time, novel optical fluence mapping algorithms and image reconstruction methods have been developed to improve the quantitative accuracy of PAT, which is crucial to recover weak molecular signals at larger depths. The development of highly-absorbing near-infrared PA molecular probes has also flourished to provide high sensitivity and specificity in studying cellular processes. This review aims to introduce the recent developments in deep PA molecular imaging, including novel imaging systems, image processing methods and molecular probes, as well as their representative biomedical applications. Existing challenges and future directions are also discussed.

Introduction

Molecular imaging provides unique opportunities for visualizing, characterizing, and quantifying biological processes at the molecular level.[1-4] With the aid of state-of-the art imaging technologies, the working mechanisms of the biological systems have been better understood in the context of living tissues, which leads to numerous advancements in disease diagnosis, drug design, and therapy assessment. Although the methodology originated from nuclear medicine (*e.g.,* positron emission tomography), which uses radiolabeled tracers that generate gamma signals from radioactive decay, molecular imaging has been generalized so that signaling from molecules is not restricted to only radioactive atoms.[1,5] X-ray computed tomography (CT),[6-8] magnetic resonance imaging (MRI),[6,9,10] ultrasound imaging (US),[11-13] optical imaging,[14,15] and photoacoustic tomography (PAT)[16-18] have all been utilized for molecular imaging. X-ray CT has high acquisition speed, high spatial resolution, whole-body penetration, and relatively low cost. However, X-ray CT uses ionizing radiation, which limits the long-term observation. MRI uses non-ionizing radiation,

and has a large penetration and excellent imaging contrast of soft tissues. However, MRI has poor sensitivity to molecular probes, which leads to a relatively long acquisition time and a large dose of contrast agent. Ultrasound imaging has high spatial and temporal resolution, relatively large penetration depth, and high portability; but it also has poor molecular sensitivity. Optical imaging has excellent spatial resolution and superior molecular sensitivity, and has been widely used in basic research to observe intracellular events in live intact cells, but

[1] Department of Biomedical Engineering, Duke University, Durham, NC, USA
[2] Department of Biomedical Engineering, University of Buffalo, NY, USA

Corresponding Authors:
Jun Xia and Jonathan Lovell, Department of Biomedical Engineering, University of Buffalo, Buffalo, NY 14260, USA.
Emails: junxia@buffalo.edu; jflovell@buffalo.edu

Junjie Yao, Department of Biomedical Engineering, Duke University, Durham, NC 27708, USA.
Email: junjie.yao@duke.edu

it suffers from poor penetration depth due to strong optical scattering in biological tissues.

PAT, also referred to as optoacoustic tomography, is a hybrid imaging modality that combines the high contrast of optical imaging with the high spatial resolution and penetration depth of ultrasound imaging.[16,19-21] In PAT, the target is illuminated by nanosecond laser pulses, and the absorbed optical energy is partially or completely converted into heat, leading to a transient local temperature rise that generates a local pressure rise and subsequently propagating acoustic waves. PAT detects the acoustic signals produced by optical absorption from either endogenous chromophores, such as hemoglobin, melanin and lipid, or exogenous contrast agents, including nanoparticles, organic dyes and reporter gene products. Since the scattering of ultrasound waves in tissue is 2-3 orders of magnitude less than the optical equivalent, PAT can generate high-resolution images in optical diffusive regime.[20] PAT is also extremely sensitive to optical absorption. A small change in optical absorption coefficient leads to the same fractional change in photoacoustic signal. Therefore, PAT has a 100% sensitivity to optical absorption contrast and is inherently capable of functional and molecular imaging. With these merits, PAT has been widely applied in diverse fundamental research and clinical practice.[18,22-25]

There are 2 major implementations in PAT: photoacoustic microscopy (PAM) and photoacoustic computed tomography (PACT).[26-30] PAM targets the quasi-ballistic and quasi-diffusive regimes with tightly/weakly focused excitation light and tightly focused single-element ultrasonic detection for direct image formation,[20,26,31,32] while PACT uses wide-field light illumination and parallel acoustic detection to image targets mainly in the diffusive regime.[33-36] PACT can be configured by using ultrasonic transducer arrays such as a linear array, ring array and 2D matrix array.[33,34,37,38] The axial resolution of PACT is determined by the detection bandwidth of the ultrasonic transducer array, and the lateral resolution is determined by the central frequency and numerical aperture. Compared with PAM, PACT typically has lower spatial resolution ($\sim$400 μm for a 5 MHz linear array) but higher imaging speed and penetration depth (up to a few centimeters). So far, PACT is the most promising for clinical translations, such as breast cancer imaging and functional brain imaging, due to its deep penetration and high compatibility with commercial ultrasound imaging systems. Thus, in this review, we will focus on the advances and applications of PACT technologies for deep molecular imaging. Readers are referred to other review articles about the PAM technologies.[28,39] In the rest of the paper, we use PAT and PACT interchangeably if not otherwise noted.

Despite the above merits, PAT also faces certain challenges. Although PAT can achieve a penetration depth of several centimeters, which far exceeds the penetration of high-resolution optical imaging modalities, it still cannot match the penetration depths of ultrasound imaging, X-ray CT and MRI. The strong optical attenuation of biological tissues is the major limiting factor of PAT's penetration depth. In addition, PAT is more sensitive to molecular contrast agents than ultrasound imaging

or MRI, but it is less sensitive than fluorescence imaging and PET.[20] Moreover, many PACT implementations suffer from 2 types of imaging artifacts: limited-view and limited-bandwidth artifacts, which often deteriorate the image quality of deep seated targets with weak signals.[40-43] Numerous efforts have been made by various research groups to address the aforementioned challenges. Through careful selection of excitation wavelength,[44-46] optimization of light delivery,[47-50] and sophisticated design and fabrication of the ultrasonic transducer,[51-55] the penetration depth of PAT has been substantially improved. Moreover, by increasing the imaging speed or frame rate, PAT can reduce the motion artifacts and improve the detection sensitivity with signal averaging, leading to larger imaging depth.[56-58] More advanced imaging reconstruction methods, such as model-based and deep-learning-based reconstruction algorithms, have been developed to further mitigate image artifacts and improve the image quality.[40,41,59-63] Moreover, the enhanced optical absorption of molecular probes has boosted the sensitivity of PAT considerably.

In this review, we describe the recent advances in improving the penetration depth and sensitivity of PA molecular imaging, focusing on 3 groups of efforts: innovative imaging systems, advanced reconstruction algorithms, and novel molecular contrast agents. In the following sessions, we first introduce various PAT technological innovations to upgrade penetration with more efficient optical excitation and acoustic detection. Next, we present advanced image reconstruction and data analysis methods to compensate for optical fluence attenuation and eliminate image artifacts. Then, we summarize the new PA-sensitive molecular probes that have superior imaging performance and functionality. Representative applications in biomedical research are also discussed. Finally, we conclude the review with a brief discussion about future improvements in molecular PAT.

Technical Advancements in Molecular PAT

Novel PAT Systems to Improve Penetration Depth

A deep-penetrating PAT system should achieve deep optical excitation and sensitive acoustic detection. To deliver more light into deeper tissues, efforts have been reported with using longer excitation wavelengths to reduce the optical attenuation, illuminating the target from the inside of the tissues, and applying wavefront shaping to focus the light in the scattering medium. To detect weak signals from deeper tissues, new fabrication procedures of piezoelectric transducers and various optical detectors have been explored to improve the detection sensitivity.

PAT with innovative light source and delivery. In conventional PAT systems, laser pulses are delivered either via free space or an optical guide to form a dark- or bright-field illumination pattern on the tissue surface.[16,20,21] Yet due to the severe wavelength-dependent attenuation of photons (*e.g.,* effective attenuation coefficient of human breast tissue is $\sim$4.0 cm^{-1} at 730 nm[64]),
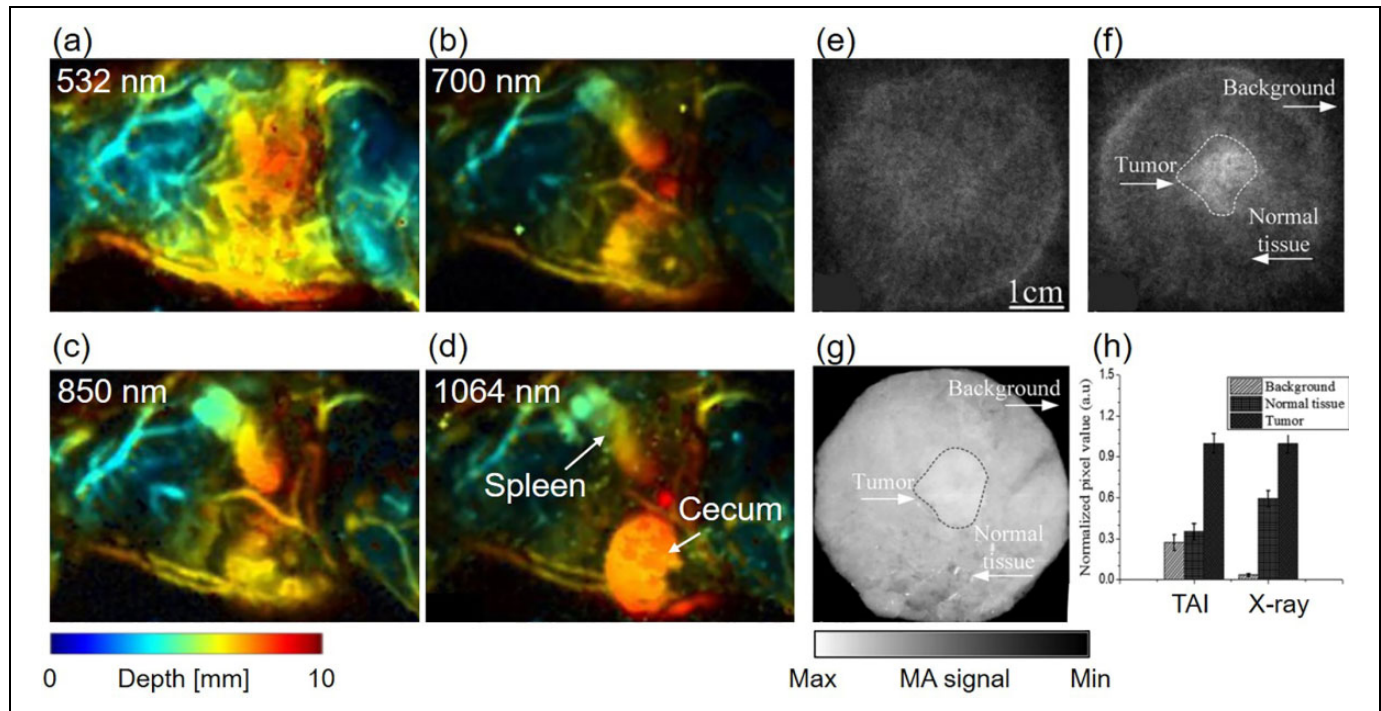
Figure 1. Deep PAT and TAT with long excitation wavelengths. (a-d) Noninvasive PA imaging of a whole-body mouse *in vivo*.[44] Depth-encoded PA maximum amplitude projection (MAP) images acquired at optical wavelengths of 532 nm, 700 nm, 850 nm, and 1064 nm. (e) TAT image of excised normal breast tissue of an ewe.[83] (f) TAT image of a breast tumor embedded in the excised breast tissue. (g) X-ray image of the tumor phantom. (h) Normalized image contrast of normal tissue, tumor, and background in the TAT and X-ray images. Reproduced with permission from.[44,83]

it remains a great challenge for PAT to penetrate beyond a few centimeters.[19] Novel light sources and delivery methods are highly desired to break the penetration limit.

Long-wavelength photoacoustic tomography. As light in the near-infrared (NIR) wavelength range has relatively low attenuation, applying longer-wavelength excitation light is often the first step in PAT to improve the penetration depth.[65] In the early days of PAT, short-wavelength light (<700 nm) was often used for imaging hemoglobin due to its strong absorption in the visible wavelength range,[19,65,66] but a depth of only a few millimeters could be imaged due to the overwhelming optical scattering at short wavelengths.[67,68] Later, NIR light (700 nm to 1350 nm) was explored due to its larger penetration depth with relatively low absorption by water.[19,44,65,69,70] For example, a penetration depth of 4 cm has been achieved *in vivo* in the human breast at 800 nm.[71] With highly-absorbing exogenous contrast agents, a penetration depth of 11 cm was achieved in chicken breast tissue.[72] Figure 1A to D compare the PA images of a mouse at 4 different wavelengths of 532nm, 700 nm, 850 nm, and 1064 nm. While the PA image at 532 nm provides mostly superficial blood vessels, organs such as spleen and cecum can be better observed at longer wavelengths.

Long wavelengths in the microwave spectrum have been employed as radiation sources in PAT to achieve greater penetration depth, a technique also referred to as thermoacoustic

tomography (TAT).[73] Unlike PAT, which relies on the optical absorption contrast, the contrast in TAT stems from tissue's dielectric properties.[74,75] In the frequency range from 0.1 to 10 GHz, the relative dielectric constant in soft tissues ranges from 5 to 70, and the conductivity ranges from 0.02 to 3 S/m, leading to a penetration depth of TAT up to 15 cm,[73,74] which is sufficient for imaging whole-body small animals and many deep organs in humans. Great progress has been made in TAT for imaging breast and prostate cancer tissues with >10 cm penetration depth. Moreover, because the dielectric properties of malignant tissues are larger than the normal tissues, the cancer tissues often have relatively strong microwave absorption than healthy tissues.[76-79] For example, breast cancer tissue has up to 10 times higher microwave absorption than normal tissues, providing high imaging contrast for TAT.[73]

Conventional TAT systems usually use high-power pulse-modulated carrier-frequency generators, and the resultant transmitted microwaves operate at frequencies ranging from 434 MHz to 3 GHz with a pulse width of a few microseconds.[80-82] The excitation pulse is prolonged to deposit more energy at the expense of spatial resolution.[46,74,76,81] To reduce the microwave pulsewidth and improve the spatial resolution, a high-voltage discharge mode has been used to generate ultrashort microwave pulses. The microwave generator uses an oscillation circuit and a Tesla transformer to generate high-voltage electrical pulses, which propagate through the antenna and radiate microwaves with a pulse energy of hundreds of
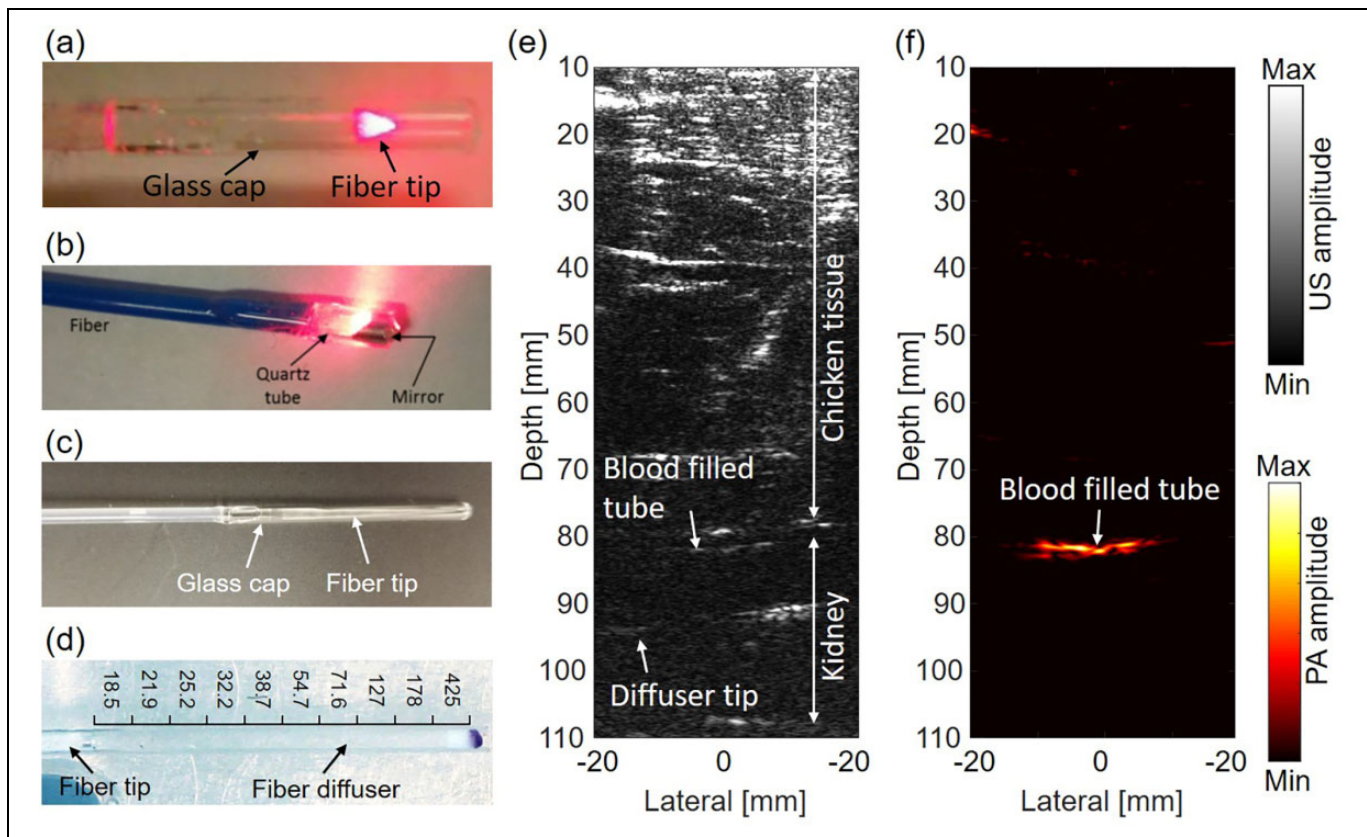
Figure 2. Internal-illumination PAT. (a) A representative forward-viewing fiber.[87] (b) A representative side-viewing fiber.[49] (c) A representative radial-emission fiber diffuser.[50] (d) A representative frontal-emission diffuser fiber diffuser. (e-f) B-mode ultrasound image (e) and PA image (f) of the blood-filled tube on an *ex vivo* pig kidney overlaid by an 8-cm-thick layer of fresh chicken breast tissue.[92] Reproduced with permission from.[49,50,87,92]

millijoules[45,75,83] and a pulsewidth of several nanoseconds. A spatial resolution of tens of microns can thus be achieved. Figure 1E to G show the TAT and corresponding X-ray images of the excised normal breast tissue and tumor tissue, respectively. The location of the tumor can be clearly imaged by TAT, with higher contrast between normal tissue and tumor tissue than that in the X-ray images (Figure 1H). Nevertheless, the microwaves used in TAT often have a low frequency (100–900 MHz), which can penetrate deeper in tissue, but may result in a lower signal-to-noise ratio (SNR). Meanwhile, it is challenging to direct microwave propagation direction.[73]

Internal light delivery. In many clinical applications, the deeply-seated organs of interest are relatively close to some body cavities. For example, the posterior boundary of an adult's kidney can be more than 10 cm from the skin surface, but the kidney is connected to the urinary tract that can be directly accessed from outside.[84] For these organs, it is therefore possible to deliver the light to the intracorporeal targets using a small-diameter optical fiber via the body cavities, largely avoiding the otherwise strong optical attenuation by the intervening tissues underneath the skin surface. Such light delivery strategy is termed as internal light illumination.

Various internal-illumination designs have been employed in PAT to deliver light to the deep organs of interest, and can be roughly classified into side-viewing illumination and forward-viewing illumination. In side-viewing illumination, the laser beam is coupled into a multi-mode optical fiber and the fiber is inserted into the vicinity region of the target. To deflect the light sideward, a 45-degree-angled prism is attached to the fiber tip or the fiber tip itself is polished with a 45-degree angle. The tip is sealed within a transparent air chamber.[49,85] In contrast, in forward-viewing illumination, the end of the optical fiber is usually sanded until the tip is beveled to a desired conical shape. Light emits from the conical fiber tip and forms a spherical illumination pattern; in other cases, light emits directly from the flat fiber tip to form a less diverged illumination.[86,87] Figure 2A and B show example designs of forward- and side-viewing fiber tips, respectively. Generally speaking, side-viewing illumination is more suitable for imaging tunnel-shaped organs, such as the gastrointestinal tract, and front-viewing illumination works better for imaging planar-surfaced organs, such as the cervix. However, both types of illumination typically cover only a small field of view, mostly because of the limited beam-diverging distance between the fiber tip and the tissue surface.
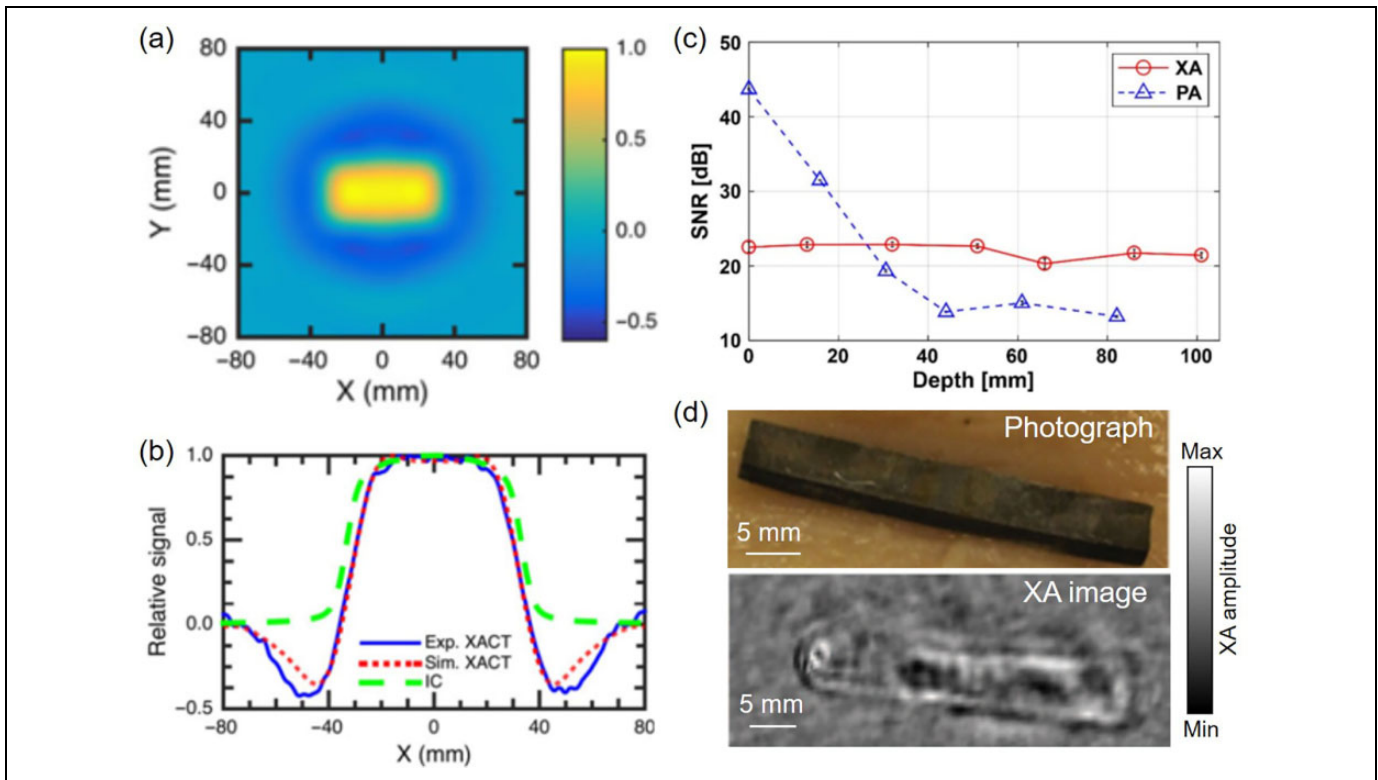
Figure 3. X-ray acoustic tomography. (a) XAI image of a 6 cm × 3 cm radiation field at 10 cm depth.[96] (b) Comparison of lateral profiles of the radiation field extracted from simulated and experimental XAI images and ion chamber measured profiles. (c) SNRs of XA and PA signals of a lead sample beneath various thicknesses of chicken breast tissues.[95] (d) Photograph and XAI image of a metal object embedded in tissue at 40.5 mm depth.[94] Reproduced with permission from.[94-96]

To illuminate a larger field of view, such as the adult kidney, Li et al have proposed to use an optical fiber diffuser for internal light delivery in PAT.[49] Two types of fiber diffusers have been explored for this purpose: radial-emission and frontal-emission diffusers. To make a radial-emission fiber diffuser, the jacket and cladding of an optical fiber are removed, and the surface of the fiber core is roughened to scatter the light out.[47,48,88] The fiber core can also be coated with a layer of optically scattering particles to further homogenize the light emission.[50,89,90] In contrast, a frontal diffuser is typically separable from the optical fiber. The diffuser is made of scattering medium, such as intralipid and TiO_2, with increasing concentrations from the fiber tip so as to generate a homogeneous light distribution in the nearby tissues.[91,92] Figure 2C and D show the representative designs of radial-emission and frontal-emission diffusers. As an example, Figure 2D shows a frontal-emission diffuser made of segmented agar mixed with intralipid. By using this fiber diffuser, the internal illumination PAT has demonstrated deep imaging on an *ex vivo* pig kidney at a depth of 8 cm, with the fiber diffuser inserted into the pig kidney through the urinary tract, as shown Figure 2E and F. Such an imaging depth is typically not attainable by traditional PAT. Internal-illumination PAT needs to use optical fibers with high damage threshold to deliver sufficient energy to the target. Therefore, there is often a tradeoff between the fiber's diameter and its flexibility. A larger-diameter fiber is less flexible and

thus may not fit for certain applications with limited space. In addition, internal-illumination PAT still suffers from the acoustic attenuation from the deep targets, especially the high frequency components, which may lead to deteriorated spatial resolutions.

X-ray acoustic imaging. Another way to increase the penetration depth of PAT is to use X-ray photons as the radiation source, which is termed as X-ray induced acoustic imaging (XAI). X-ray photon scattering in tissue is much lower than that of visible-NIR photons.[93] Several groups have reported XAI systems that include a linear accelerator (LINAC), an ultrasonic transducer (array), and a data acquisition system.[94-96] The X-ray pulses generated by the LINAC typically consist of picoseconds pulse trains and has a total pulsewidth of a few microseconds.[95] The amplitude of an X-ray-acoustic (XA) wave is proportional to the X-ray photon absorption, which is more prominent in high-density materials such as lead blocks, bones, and microcalcifications.[96] An ultrasonic transducer, which typically has the central frequency of less than 1 MHz, is used to acquire the generated XA signals.[94,97,98] One common application of XAI is to provide dosimetric information during radiation therapy.[95-97] Figure 3A and B show the XAI map of a 6 cm×3 cm radiation field at 10 cm depth in water, demonstrating that the XA intensity is closely related to the deposited X-ray dose.[96] Compared with traditional PAT
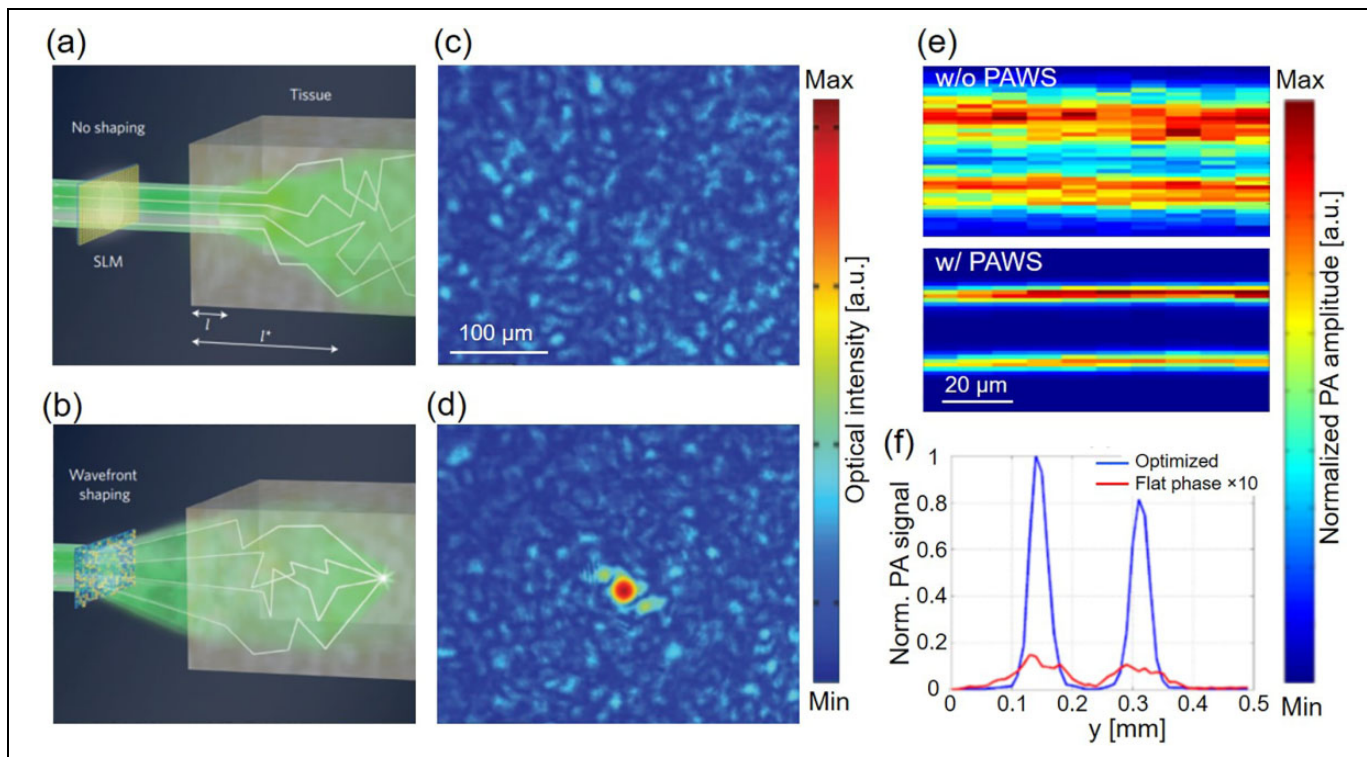
Figure 4. PAT enhanced by wavefront shaping. (a) Principle of a phase-unmodified coherent beam of light travels into tissue.[107] (b) Principle of beam refocusing by wavefront-shaping the incident light field with an SLM.[115] (c) Representative transmission micrograph with an unshaped incident beam. (d) Representative transmission after optimization for beam focusing. (e) PA imaging of 2 capillary samples without and with applying wavefront shaping. (f) PA profiles across the capillary tubes with and without wavefront shaping.[116] Reproduced with permission.[107,115,116]

using visible-NIR light, XAI has superior penetration depth in tissues due to the weak X-ray scattering.[95] As shown in Figure 3C, while the PA signals rapidly decreased with the depth, XA signals only slighted decreased up to 10 cm. However, compared to visible-NIR laser pulses, X-ray pulses are much longer, which leads to a lower X-ray acoustic conversion efficiency and degraded spatial resolution.[21,99] To improve the resolution and SNR of XAI, Xiang et al used an X-ray tube to produce nanosecond pulses and achieved an $\sim 300\,\mu m$ resolution.[99] Ultrasonic transducer arrays were also used to achieve high-speed 3D XAI.[98] Nevertheless, one major concern in XAI is the ionizing radiation exposure.[100] It has been reported that the minimum dose required to obtain an XAI field image in water is 11.6 mGy, with an SNR of 6.4,[97] which is comparable to a typical chest X-ray CT dose of 12-18 mGy. It is promising that XAI can provide clinically meaningful images at low doses.

Wavefront shaping enhanced light delivery. PAT's penetration depth in tissues can be enhanced by employing wavefront shaping techniques. Wavefront engineering technologies have enabled refocusing light inside scattering medium by compensating for or reversing the scattering-induced phase scrambling, based on the fact that optical scattering is microscopically deterministic and time-reversible in nature.[101-105] In a typical wavefront shaping implementation, a spatial light modulator

(SLM) is used to optimize the phase of input light by using a guide star as the signal feedback,[106-108] as shown in Figure 4A and B. Doing so, the light intensity in deep scattering medium can be enhanced by more than 1000 times (Figure 4C and D). Many types of guide stars have been reported, including fluorescent labels,[109,110] nonlinear optical particles,[111] as well as photoacoustic and ultrasound targets.[102,103,112,113]

PAT is advantageous over fluorescence imaging for providing wavefront shaping feedback signals, since PAT can penetrate relatively deep. Via wavefront shaping, maximizing the PA signal strength will lead to maximizing the local optical fluence within the ultrasound detection zone,[102,103,114] which in turn increases the penetration depth of PAT. An enhancement of $5 \sim 10$ fold in the PA signal strength has been reported by Kong et al after wavefront optimization.[114] Figures 4E and F show the enhancement of photoacoustic imaging with wavefront shaping (PAWS), in which both the SNR and spatial resolution were substantially improved. However, so far, most wavefront shaping technologies are still too slow for *in vivo* PAT applications, due to the fast optical speckle decorrelation induced by the tissue motion and blood flow. Further improvement in the wavefront shaping speed is still needed, such as by accelerating the phase optimization process.

PAT with ultrasensitive and fast ultrasonic detection. Another important factor that affects the penetration depth of PAT is

the sensitivity of the ultrasonic detection. A highly sensitive ultrasonic transducer is able to detect weak signals from deep-seated chromophores near which light has been severely attenuated. The sensitivity of an ultrasonic transducer is usually assessed by its noise equivalent pressure (NEP) with units of *Pa*, which reflects the minimum detectable photoacoustic signal pressure.[39,117] A lower NEP is desired for a more sensitive ultrasonic transducer.

Sensitive PZT transducers.. Piezoelectric transducers are most widely used for acoustic detection in PAT, and have demonstrated the best sensitivity. For example, a piezoelectric transducer with a detection area of 30 mm^2 and a bandwidth of 50 MHz has achieved an NEP of ~ 77 *Pa*.[118] The detection sensitivity of a traditional piezoelectric transducer can be improved by further increasing the active element area and decreasing the detection bandwidth.[39] However, both measures lead to reduced PAT image quality. First, it is technically challenging to fabricate ultrasonic transducer arrays with large elements, which also suffer from reduced directivity and strong grating lobes.[119] Moreover, miniaturized ultrasonic transducers are often needed for photoacoustic endoscopy in order to access the intracorporeal organs.[120-124] Second, a broadband detection bandwidth is preferred in PAT to achieve high spatial resolution and reduce limited-bandwidth artifacts.[16,125] Although high-frequency ultrasonic waves are attenuated more strongly by tissues, a broadband transducer is still highly desired to detect the deep-seated small targets.[19]

Recent advances in ultrasonic transducer fabrication has shown that the loss of sensitivity with a small element size can be mitigated in capacitive micromachined ultrasonic transducers (CMUTs) and piezoelectric micromachined ultrasonic transducers (PMUTs).[126-130] The basic building block of CUMT is a capacitor cell, which consists of a thin, movable plate suspended over a vacuum gap on top of silicon substrates. CMUT uses semiconductor fabrication techniques, such as the wafer bonding and sacrificial release processes. The metal layer on the plate or the plate itself serves as the top electrode of the capacitor, and the conductive substrate acts as the bottom electrode. After connecting to a constant bias voltage, an electrical current is generated when ultrasound pressure waves hit the movable top plate that leads to a change in capacitance.[128,129,131] PMUTs have similar structures with CMUTs, in which an array of sensitive micro-piezoelectric membranes are formed on the silicon substrates.[55,126,127] It has been experimentally demonstrated that row-column-addressed 2D CMUTs have wider reception fractional bandwidth than classic piezoelectric transducers with similar acoustic features (*e.g.*, dimension, central frequency, packaging). Compared with traditional piezoelectric transducers (PZT), one strength of CMUTs and PMUTs is the potential high-throughput batch manufacturing, which can drastically reduce the unit cost and benefit the fabrication of inexpensive 2D arrays. The sensitivity of CMUTs, however, is not necessarily higher than conventional PZT transducers, and it can be possibly improved by optimizing the structure, plate design, layout, and driving conditions.[54,130]

Optical detection of ultrasound waves. Optical techniques are becoming increasingly popular for PA signal detection, since they have several advantages over traditional piezoelectric transducers. The sensitivity of optical sensors is independent of the detector size, and their bandwidths are usually much wider.[125,132,133] As a result, with the same element size, optical detectors typically provide greater sensitivity over a significant wider frequency range than its piezoelectric counterpart, which is particularly attractive for PA endoscopy or 3D PAT.[51,134,135] In addition, the transparent nature of optical detectors simplifies the light delivery in PAT.[51] However, when the transducer element size is not a constraining factor, piezoelectric transducers still provide a higher sensitivity. Here we introduce several representative optical detection of ultrasound waves, including Fabry-Pérot (FP) interferometers,[132,136] micro-ring resonators,[52,134,137] and fiber Bragg gratings.[53,138]

Fabry-Pérot interferometers (FPI) use transparent planar FP polymer films as acoustically sensitive elements. The PA excitation light can transmit through the films into the underlying tissue. The resultant ultrasound waves modulate the thickness of the FPI. A CW interrogation beam reads the FPI thickness and records the PA signals.[136] FPI sensors have much higher sensitivity than PVDF receivers with a similar element size: a 75-µm diameter PVDF receiver has a typical NEP of 55 *kPa*, while an FPI with a 64-µm diameter has a NEP of only 0.31 *kPa*. A -3 dB detection bandwidth of a 22-µm-thick FPI ranges from 0 to 39 MHz, which is sufficient to detect deeply located targets. Zhang et al have reported an improved FPI sensor using a plano-concave optical microresonator, which comprises a solid plano-concave polymer microcavity formed between 2 highly reflective mirrors, as shown in Figure 5A.[132,139] The interrogation CW laser beam is then tightly focused by the top mirror curvature, which is precisely designed to perfectly match the beam divergence and avoid the beam from walking off as it does in the planar FPI.[132] A high degree of optical confinement can then be achieved and eventually lead to a much improved detection sensitivity: the NEP of a 100-µm plano-concave microresonator is 13.75 *Pa*, which is comparable to the NEP of a 2 mm PVDF needle hydrophone. Figure 5D and E show PA images of mouse abdominal skin microvasculature using an endoscopic FPI probe with a diameter of 3.2 mm. The high image quality has demonstrated the possibility of all-optics methods for deep PAT.

Micro-ring resonators (MRR), which consist of a bus waveguide and a ring-shaped resonator separated by a low-dielectric gap, are also useful for optical detection of ultrasound waves. The light transmitted through the bus waveguide can be evanescently coupled into the ring resonator across the gap to form strong optical resonance inside the ring, in which the stop band or zero transmission is achieved at the resonant frequency. The deformation of the ring resonator by the ultrasound wave can cause changes in the optical path length and thus a shift in the resonant frequency.[52] The design of an MRR detector is shown in Figure 5B. Li et al have demonstrated that the NEP of a 60-µm-diameter MRR can achieve as low as 6.8 *Pa* with a 140 MHz bandwidth. Figure 5F and G show the volumetric
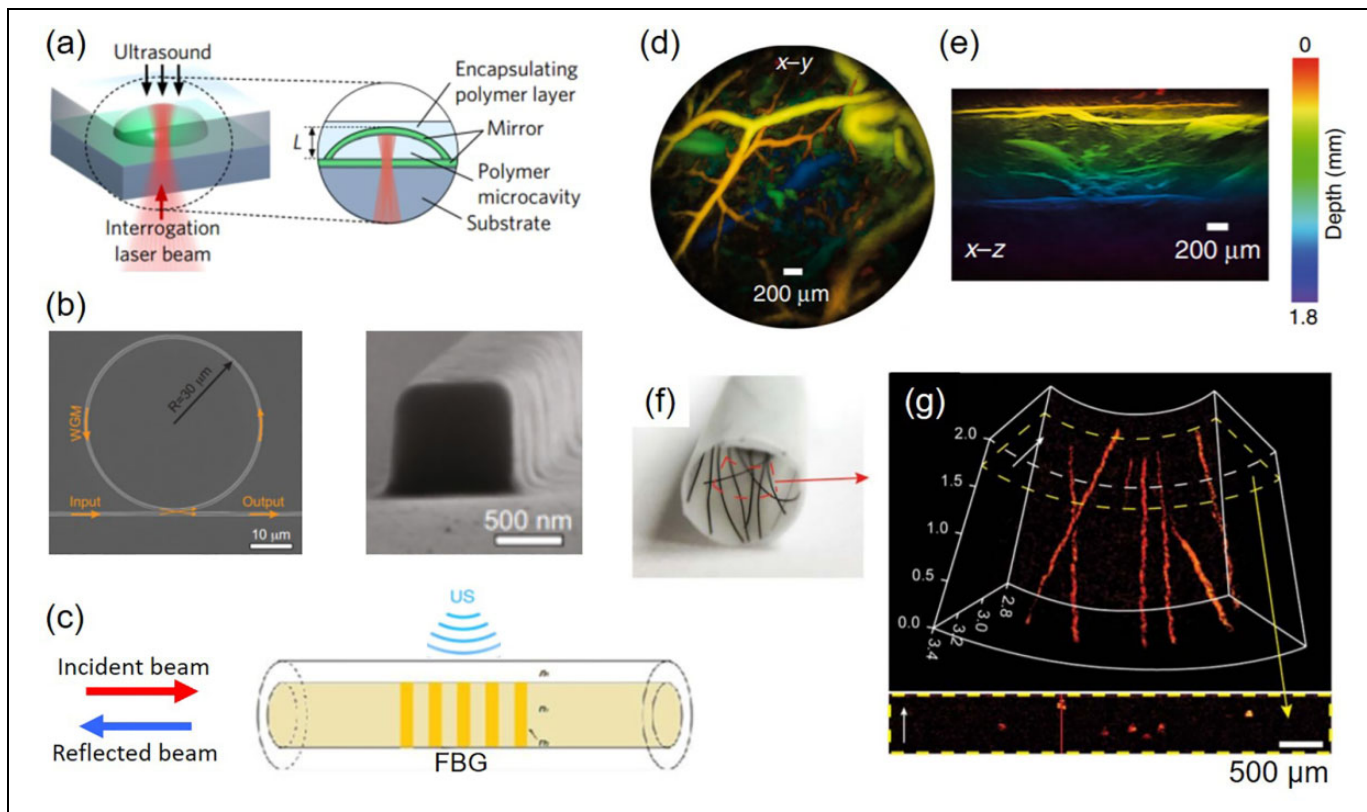
Figure 5. PAT with optical detection of ultrasound waves. (a) The schematic of a plano-concave FPI microresonator.[132] (b) Scanning electron micrograph of the MRR (left) and one cross-section of the ring (right).[52] (c) Geometry of fiber Bragg gating (FBG) detector.[138] (d-e) PA images of mouse abdominal skin microvasculature using a forward-viewing FPI probe.[51] (f) Photograph of a hair phantom. (g) Volumetric rendering of the PA imaging of the hair phantom by an MRR detector. The cross-sectional view of the dashed region is shown in the bottom panel.[134] Reproduced with permissions from.[51,52,132,134,138]

PA imaging of human hairs sandwiched by 2 tube walls, acquired by an MRR sensor. However, MRR typically provides a broad bandwidth only with a small acceptance angle, which is not ideal for parallel acoustic detection in PAT.[125]

Fiber Bragg grating (FBG) detectors fabricate Bragg gratings inside the core of an optical fiber.[53] When the wavelength of the incident light satisfies the Bragg condition, the reflection from all gratings interfere constructively, resulting in a narrow dip in the transmission optical spectrum. The ultrasonic wave-induced mechanical perturbation creates changes in the grating period and leads to a shift in the Bragg wavelength and thus change in the light transmission. The geometry of an FBG detector is shown in Figure 5C. By detecting the frequency shift of the beating signal between the 2 orthogonal polarization modes induced by photoacoustic waves in the FBG based detectors, Liang et al have reported that the FBG detector can achieve a NEP of 40 Pa and a bandwidth of 50 MHz, with a fiber diameter of 65 μm.[140]

High-speed PAT. High-speed PAT is advantageous for (pre)clinical applications, due to reduced motion artifacts, real-time feedback, and possible signal averaging. The imaging speed of traditional PAT systems is often limited by the low pulse repetition rate of powerful Nd: YAG lasers. With a kilohertz pulse repetition rate, laser diodes have been explored as the excitation light source in high-speed PAT, and a large number of frames can be acquired in a short time.[141,142] However, the low pulse energy is currently the major drawback of laser diodes. Furthermore, with a large number of transducer elements, traditional PAT suffers from the time-consuming data transfer and image reconstruction, preventing real-time imaging. To address this issue, compress-sensing based PAT has been developed by using only a small number of transducer elements and incorporating total variation in the image reconstruction.[58,143] Real-time 3D PAT has been achieved by Ozbek et al, with a highest frame rate of 1.6 kHz and a spatial resolution of 75 μm.[57]

Novel Imaging Reconstruction and Signal Processing Methods

Reconstruction algorithms are essential for PA images with high SNR, high resolution, and low artifacts, especially when reconstructing PA images with weak signals from the large depth. In this section, we discuss innovations in PA molecular imaging as it pertains to penetration depth, reconstruction accuracy, and detection sensitivity.
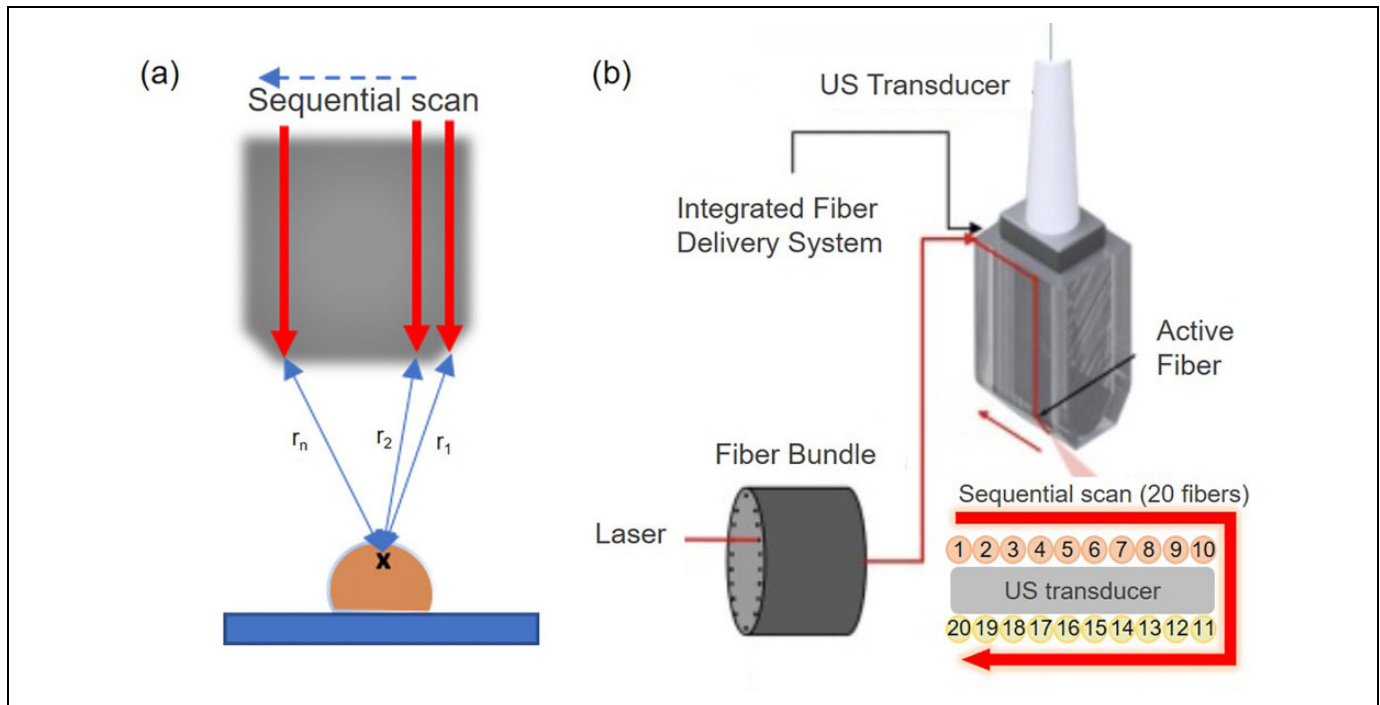
Figure 6. Spectroscopic PAT with simultaneous fluence compensation and motion correction. (a) Fluence compensation through a "fast-sweep" sequential illumination technique. Light emitted from different fibers propagates different distances to the target located within tissue. (b) Sequential illumination in PA/US system. These measurements are used for robust estimation of the laser fluence in the medium independent of the wavelength. The procedure is repeated for all wavelengths used in the experiment. Reproduced with permission.[149]

Fluence compensation. The initial PA pressure amplitude is directly proportional to the absorbed optical energy, which is a product of optical fluence and optical absorption coefficient in tissue. Therefore, the generated PA image is heavily dependent on the local optical fluence, especially for deep tissue imaging applications. Biological tissues are highly scattering media for visible-NIR photons. As the imaging depth increases, optical fluence tends to decrease exponentially even in a homogenous medium. Due to the heterogeneous nature of biological tissues, modeling light fluence in tissue is complicated. Some groups have developed PAT and diffuse optical tomography (DOT) dual-modality systems to compensate for light fluence variation and achieve more accurate reconstruction of optical absorption coefficients.[144-146] However, these systems are bulky as they require different illumination and detection equipment for each modality. Fluence compensation has been a major challenge in quantitative PAT of blood oxygenation and other exogenous molecules. In this section, we introduce the most recent advances in this field. Earlier developments in the area can be found in review articles.[24,147]

Hussain et al have proposed a method for fluence compensation using ultrasound-enabled, non-invasive tagging of light at the region of interest.[148] As ultrasound scattering in tissue is negligible in comparison to optical scattering, the ultrasound beam can be well focused at the region of interest. When tissue is illuminated with a coherent light beam, the photons are scattered out of the tissue and form a speckle pattern. The fluence map can be obtained by scanning the focused ultrasound to measure the speckle contrast. The fluence measurement is directly integrated into a PAT system such that the fluence maps and PA images can be obtained simultaneously. The feasibility of this method was assessed in agar and intralipid models, porcine tissue samples, and sO_2 measurements. Imaging results from sacrificed mice indicate that there was an improvement in fluence compensated images compared to images without fluence compensation. However, this method has yet to be tested for *in vivo* applications in which complex tissue dynamics come into play. Furthermore, this technique requires the use of 2 separate lasers and point-by-point scanning, which makes the system more complex and increases the imaging time (approximately 29 min for an area of 530 mm^2).

Kim et al have developed a real-time, spectroscopic PA/US system with simultaneous fluence compensation and motion correction.[149] For PA acquisition, a single image is formed by sequential scanning using a narrow laser beam through fiber sweeping (called "fast-sweep"). Light from different fibers propagates different distances in tissue. The partial PA image reconstructed from a single fiber illumination is used to estimate the signal loss due to light attenuation (Figure 6). This method allows the estimation of laser fluence for the targeted absorber. This procedure is repeated over 10 wavelengths in the range of 700-900 nm. The final image is formed by a coherent summation of partial images at a video rate of 50 Hz. The method was tested on *in vivo* mouse models for monitoring drug delivery using gold nanorods. Using this "fast-sweep" approach, the system footprint and cost are reduced. However,
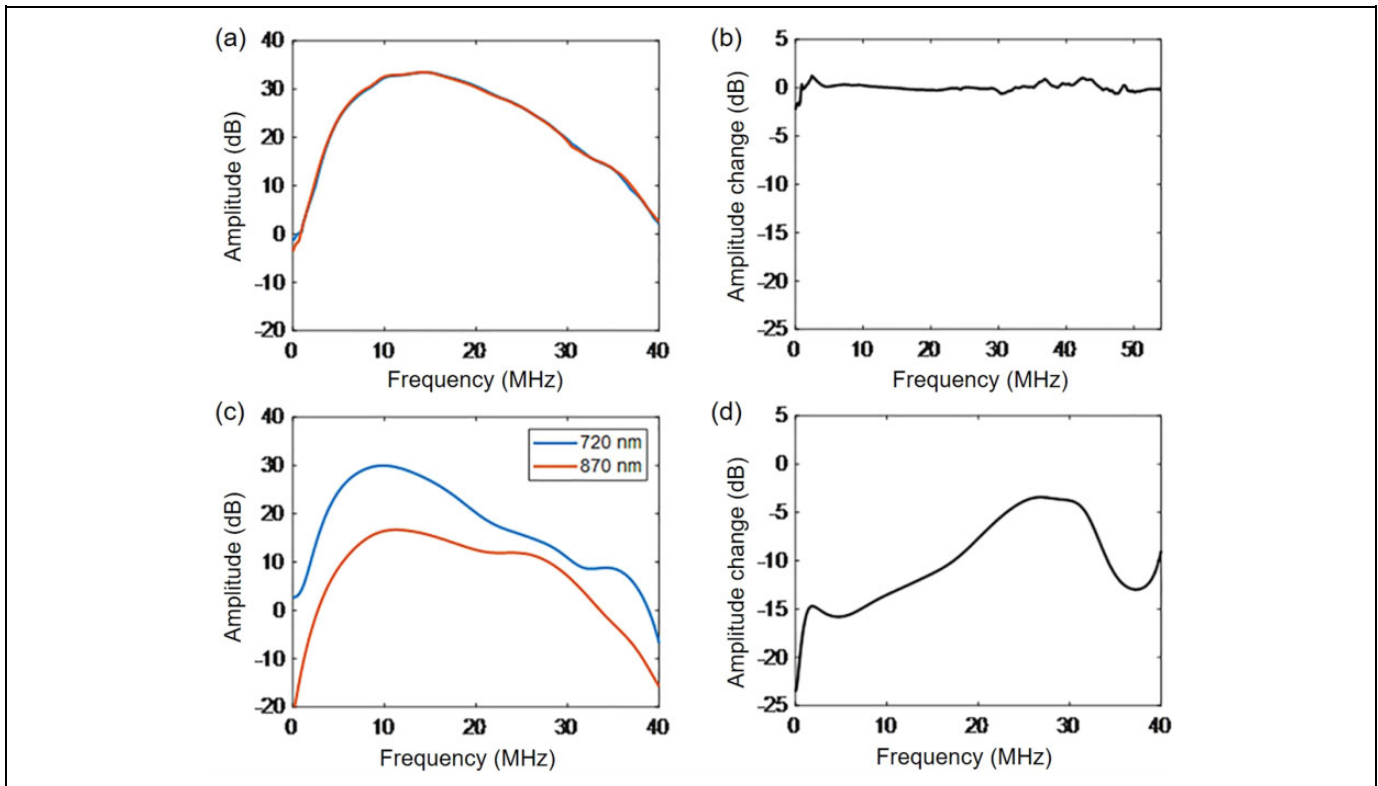
Figure 7. Fluence compensation using the PA signal power spectra. (a, c) PA signal spectra of a gold-plated microscope slide, acquired at 720 nm and 870 nm, in clear medium and scattering medium, respectively. (b, d) The ratio of the 2 signal power spectra in (a, c), respectively. Reproduced with permission from.[151]

a major drawback of this system is the slow imaging speed, which suffer from motion artifacts for *in vivo* cases.

An integrated PAT system with diffuse reflectance imaging has also been developed by Jin et al.[150] This system utilizes a single piezoelectric transducer that receives both PA waves and passive ultrasound (PU) waves. The absorbed photons by the tissue generate PA signals, while the reflected photons generate PU waves. For fluence compensation, the relationship between the PU wave amplitude and light penetration is calibrated. After calibration, the absorption differences caused by optical fluence variation can be corrected. The compact design of this system allows integration of various deep imaging applications. However, the calibration method used to estimate the relationship between PU amplitude and light fluence may not be available for all applications.

The fluence compensation can also be realized by matching the spectra profiles of PA images acquired at different wavelengths.[151] The key assumption in this method is that optical diffusion affects the power spectra of PA signals. When there is no optical diffusion, the PA spectra follow the same frequency distribution (Figure 7A), regardless of the light wavelength (Figure 7B). Adding the scattering material leads to a broadening in PA signal spectrum (Figure 7C), which is also light wavelength dependent (Figure 7D). Frequency filters are used to correct the frequency domain signal and thus the optical fluence. Although this work was developed to quantify sO_2,

this concept may be extended for molecular imaging as well. However, this approach was validated only using a very thin phantom and murine muscle model; therefore, its applications for deeper tissues is unclear. Moreover, the linear fit for the power spectra ratio may not be valid for certain geometries.

Eigenspectrum methods for signal unmixing. In PAT, to estimate different chromophore concentrations, whether it is for endogenous or exogenous contrast agents, a linear spectral unmixing method is commonly used to separate the signals from different chromophores. However, in deep tissue, the linear spectral unmixing method fails due to spectral coloring induced by wavelength-dependent optical attenuation.[147,152,153] Eigenspectrum-based methods have been recently proposed to address this issue by converting the fluence correction problem from the spatial domain to the spectral domain. By modeling light fluence as a linear combination of eigenspectra, the fluence can be corrected with improved accuracy.

The eigenspectra method was initially proposed in multispectral optoacoustic tomography (eMSOT).[154] The method is based on the fact that light fluence spectra at different locations in tissue is a cumulative result of light absorption from various tissue chromophores. Thus, the fluence spectrum can be expressed as the linear combination of some base spectra (one mean fluence spectrum and 3 eigenspectra), determined through principal component analysis (Figure 8). It was
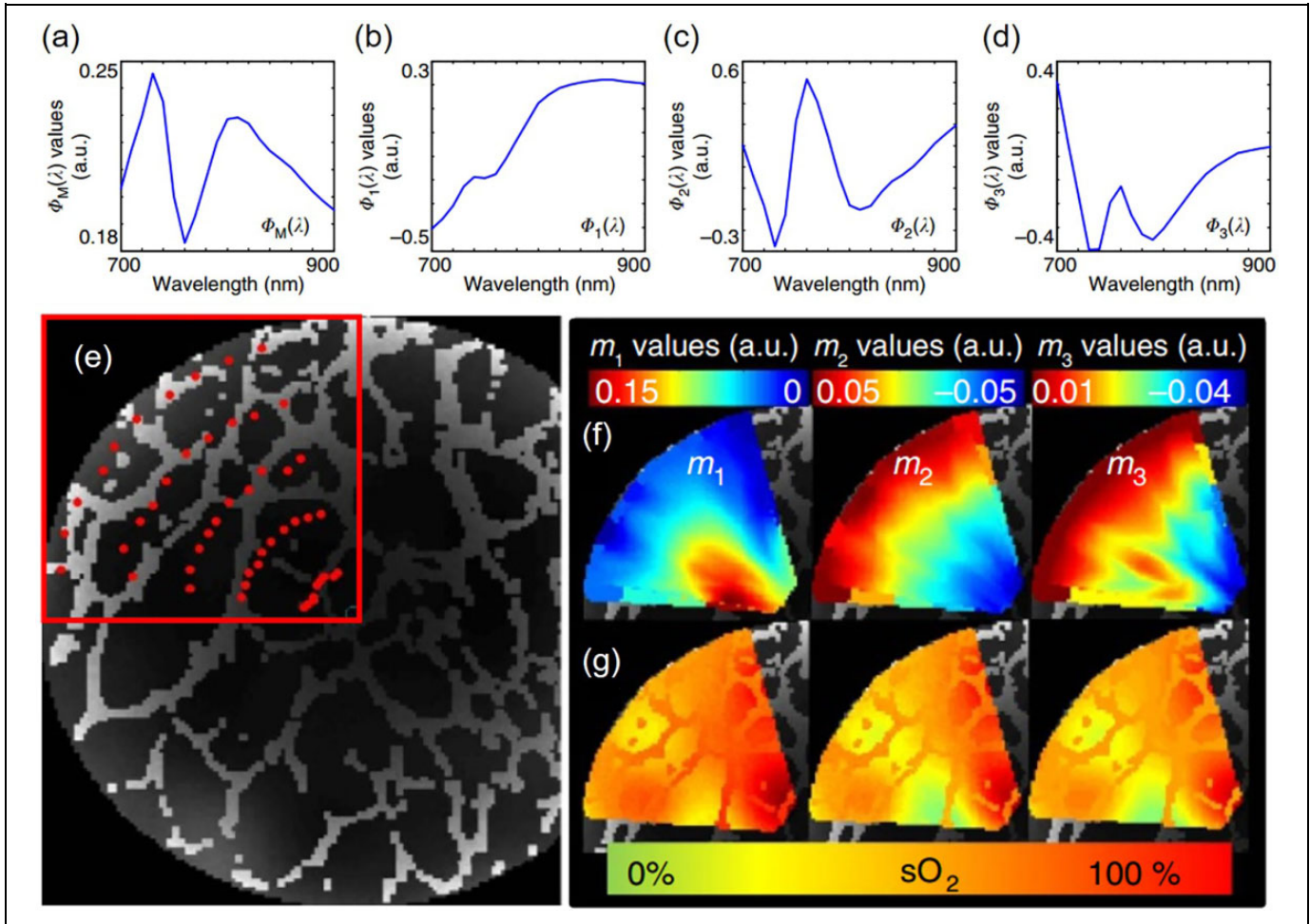
Figure 8. eMSOT for optical fluence correction. (a-d) The eigenspectra model composed of a mean fluence spectrum (a) and 3 fluence eigenspectra (b-d). (e) Application of a circular grid (red points) for eMSOT inversion on an area of a simulated PA image. (f) Maps of model parameters used to spectrally correct the original PA image. (g) sO$_2$ estimation using linear unmixing (left), eMSOT (middle), and the gold standard (right) of the selected region. Reproduced with permission from.[154]

observed that the first eigenspectrum was associated with the "spectral shape" of light fluence that related to the average blood oxygenation of the surrounding tissue, while the second eigenspectrum was associated with the changes in depth of light fluence and the average optical properties of the surrounding tissue.[154] *In vivo* and *postmortem* studies were used to validate these observations. The sO$_2$ estimation can be made independent of the tissue's optical properties. However, the accuracy of eMSOT is prone to noise and artifacts. Based on Bayesian inversion, Olefir et al described a method to improve eMSOT for spectral unmixing in noisy environments.[155] With this method, spectra can be weighted automatically based on their reliability. However, this new method still needs improvement in speed as it is currently $\sim$ 12 times slower than eMSOT. Also, this new method needs to be tested for absorbers other than hemoglobin for molecular imaging applications.

Model-based 3D reconstruction methods. Although filtered-back projection (FBP) has been widely used in PAT,[156] it does not account for many important factors of the imaging system, such as the impulse and spatial response of the ultrasonic transducer, limited-view detection, as well as thermal and electronic noise. Also, in deep tissues, there exist spectrally derived artifacts. All these factors impact the quantitative accuracy of the molecular imaging.

Many groups have been developing model-based methods to address the above issues.[157] Prakash et al have developed a logarithmic, regularization-based, entropy maximization algorithm to improve the quantitative performance of PAT.[158] Entropy maximization is used prior to PA image reconstruction,[159,160] with an implicit non-negativity constraint. This method is superior than conventional *l*2-norm minimization.[161] However, entropy evaluation with limited independent data still needs to be investigated for clinical translation, as most clinical systems use linear ultrasound transducer arrays with relatively small detection angles.

Mastanduno and Gambhir have proposed a model-based tomographic method to map tissue absorption based on the
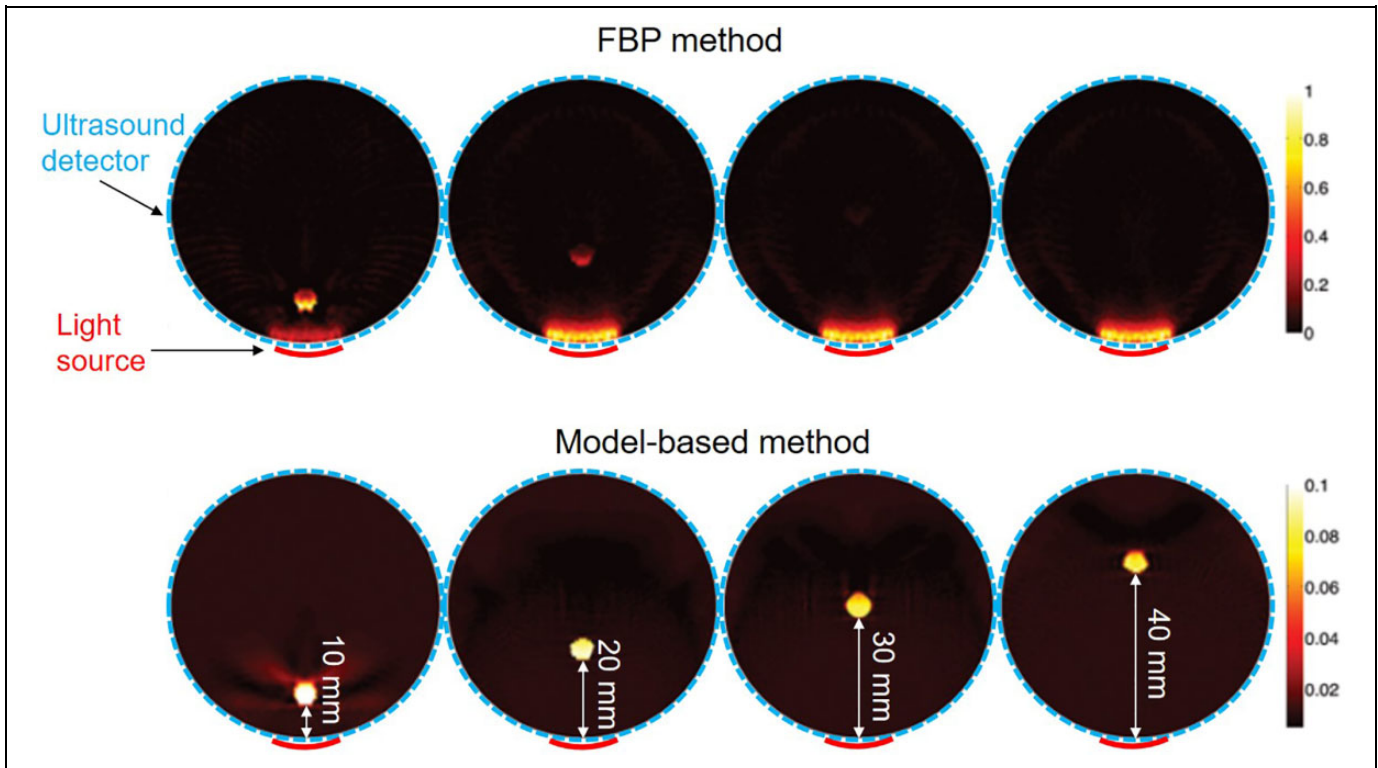
Figure 9. Model-based image reconstruction of absolute optical absorption on a numerical phantom with a 5 mm-diameter target. The optical source is located at the bottom of the circle (red), and a ring-shaped ultrasound transducer array is around the entire phantom (blue). The target depth is varied from 10 mm to 40 mm, and the PAT images are reconstructed by the FBP method (top row) and model-based method (bottom row). Reproduced with permission from.[162]

acoustic data only, with no prior knowledge of optical properties, initial pressure distributions, or tissue structure.[162] Using the optical diffusion model and k-space acoustic model, absolute absorption coefficients are reconstructed iteratively.[163] As shown in Figure 9, this method was able to recover the target's absorption with an error of up to 22% at 4 cm depth. Although this method showed remarkable improvement over FBP, its performance remains to be tested on real biological tissues.

Deep learning-based reconstruction methods. Model-based reconstruction methods, although more accurate than the FBP method, are computationally expensive for practical use.[18,23] Deep learning, a rapidly emerging research area focusing on pattern recognition and machine learning techniques, has recently found applications for biomedical imaging.[164-166] In a typical deep-learning algorithm, the artificial neural network represents the non-linear relationship between the input and output images, and the algorithm performs various optimization processes at different layers based on the training datasets.[167] Recently, several groups have adapted deep learning methods to address the limited-view and under-sampling issues in PAT.[40,59,168-170] Here, we will focus on several examples for quantitative PAT reconstruction.

Bench et al have demonstrated the feasibility of 3D convolutional neural networks to generate accurate sO$_2$ maps, by using the full spatial information contained in the 3D PA images.[171] Two convolutional encoder-decoder networks with skip connections (EDS) were trained to output 3D sO$_2$ and vessel segmentation maps. However, the network accuracy decreased with depth, due to decreased SNR and/or limited view.

A residual learning framework (ResU-net) was also employed for PAT.[172] ResU-net takes PAT images acquired at different wavelengths as the input and generates sO$_2$ maps or molecular concentration images as the output. The residual learning mechanism can prevent accuracy degradation that commonly happens with increasing network depth. Figure 10A to C show the estimated indocyanine green concentration using ResU-net, demonstrating great promise for molecular imaging applications. However, its performance on animals remains to be investigated.

An U-net based architecture was developed for PAT to directly recover the optical absorption from the deposited energy distribution.[173] The training data was generated from Monte Carlo simulation of light transport with wide-field illumination. This method has been validated on circular targets of different sizes and positions (Figure 10D-F). The relative error with different absorption backgrounds was less than 10%. Again, more complex experiments are necessary to demonstrate its feasibility for biological applications.
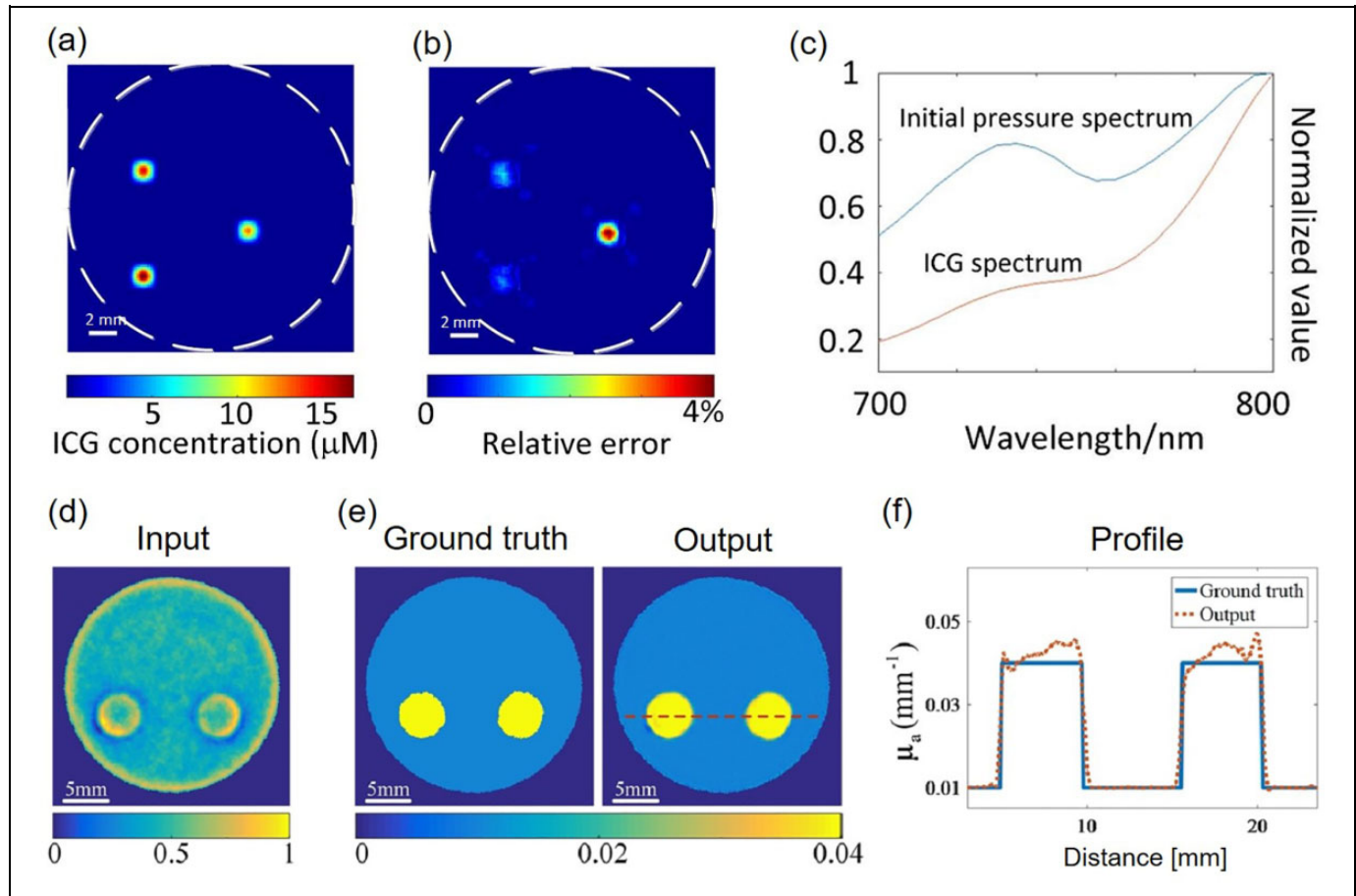
Figure 10. PAT image reconstruction based on deep learning. (a, b) ResU-net is used to estimate the absolute concentrations of indocyanine green. The reconstruction error relative to the true concentration is <5%. (c) Normalized true molar extinction coefficient and the measured PA spectrum of the rightmost target in (a-b).[172] (d-f) U-net based network is used to estimate the absorption coefficients of the targets.[173] Reproduced with permission from.[172,173]

Novel Molecular Probes for Deep PAT

The use of molecular probes with high optical absorption is another way of extending the penetration depth of PAT. Recently there have been significant advancements in the formulation and evaluation of organic dyes and nanoparticles that absorb light between 1000-1700 nm, which is known as the NIR-II region. The NIR-II region is noteworthy due to it deeper tissue penetration with PAT, with minimal interference from endogenous tissue components such as hemoglobin and water. Several interesting PAT contrast agents have been developed with NIR-II activity. Additionally, novel genetic probes and activation sensing probes have shown their potential for PAT applications.

Inorganic probes. Inorganic probes have the advantage of being highly adjustable in size and absorption bandwidth, and are typically formed from metals or unnatural molecular structures. These customizations allow for alterations that can modulate the optical properties and pharmacokinetic behaviors. Historically, inorganic contrast agents have been used extensively in PAT. In particular, gold and carbon nanotubes have shown great potential for strong PA contrast. One application involved targeting the

lymphatic system in mice with an antibody conjugation to the gold plated nanotubes.[174] Another study conjugated a tumor specific peptide to the gold nanorods on the surface of carbon nanotubes to target gastric cancer cells.[175] This technique is potentially generalizable to other types of cancer cells.

Gold nanoparticles have historically been used in the NIR-I region.[176] In the longer NIR-II region, improved signal to background ratio (SBR) improves PA imaging.[177] One study with small gold nanorods that absorbed light in the NIR-II region led to strong PA signal in tumors in mice as well as higher thermal stability relative to larger counterparts. With small gold nanorods that absorbed light in the NIR-II region, PAT can image tumors more effectively. Figure 11 shows that peptide targeting in combination with small gold nanorods can be used to effectively image tumors with high contrast.

The customizability of inorganic probes makes them useful for mapping tumor vasculature using quantum dots comprised of polymers and silver[178-180] as well as different polymer coated metal mixtures: Cd, Te, Mn, and Hg.[181,182] The main PAT application is imaging tumor angiogenesis. Quantum dots can absorb in both the NIR-I and NIR-II regions, which
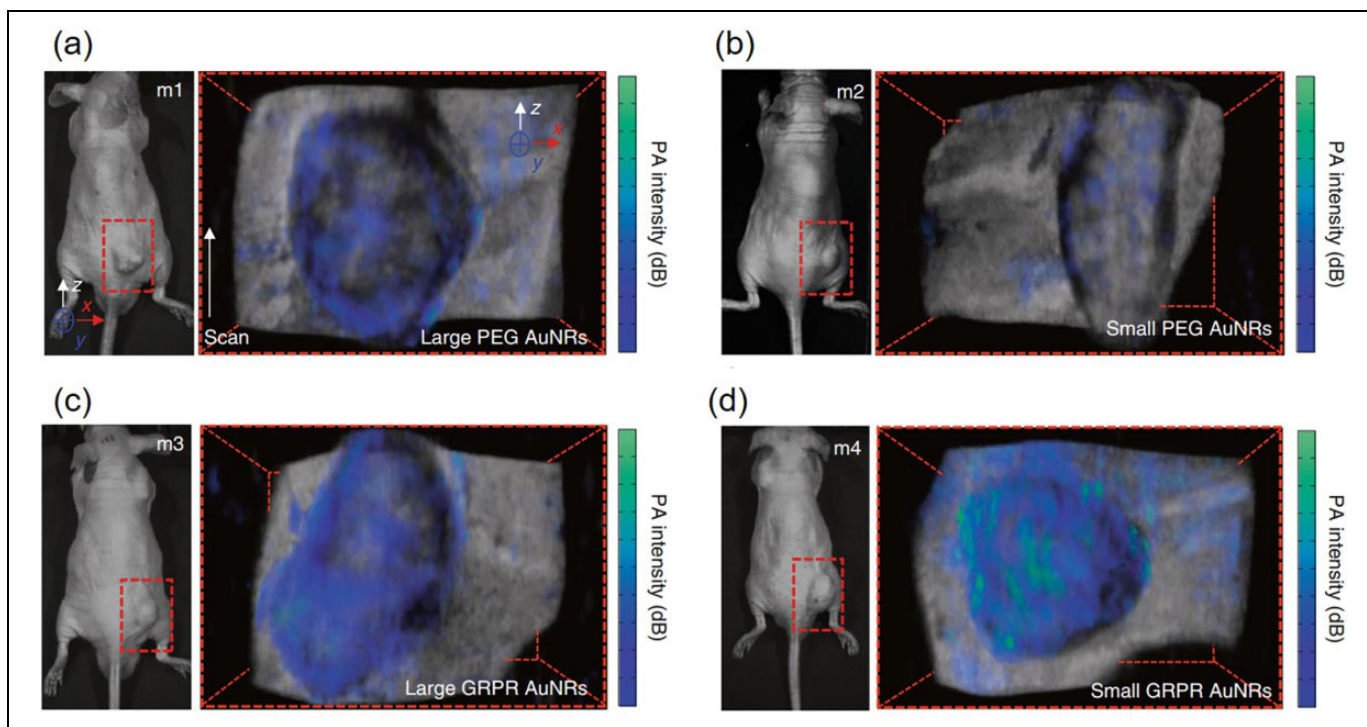
Figure 11. PAT of targeted small and large gold nanorods (AuNRs) in a murine model of prostate cancer. (a-d) Photographs (left) and PAT images (right) of tumor-bearing mice with non-targeted large (a) and small (b) AuNRs and with peptide targeted large (c) and small (d) AuNRs. The PA signal intensities are displayed in color, overlaid with the ultrasound images in gray for anatomical information. Reproduced with permission from.[177]

presents the potential for multispectral PA imaging.[179,180] The advantages of quantum dots for PA molecular imaging include high stability, stronger absorption, and longer circulation times due to the polymer coating and custom sizing to evade renal clearance. The main disadvantage of quantum dots is their toxic side effects. Efforts to minimize tissue accumulation must be realized before clinical translation.[183]

Organic dyes and nanoparticles. Organic dyes and nanoparticles are noteworthy probes because they tend to be biocompatible, with the possibility of biodegradation. One formulation of cyanine fluoroalkylphosphate salt (CyFaP), an NIR-II dye that achieves imaging in deep tissues, is a micelle formed with surfactant stripping. This formulation was successful used in PAT at a 12 cm depth through chicken breast tissue as well as imaging through 5 cm of human breast tissue in adult volunteers,[184] as shown in Figure 12.

New NIR-II organic dyes are rapidly developed in order to exploit the advantages of deeper penetration, less tissue scattering, and permissible use of higher laser powers of longer wavelength. Often, organic dyes need to be solubilized with a surfactant of polymer matrix due to their hydrophobic nature.[185] Bright NIR-II signal is achievable using organic dyes,[186,187] some of which have fast renal clearance.[188] Modifications can be made to the dyes to narrow the absorbing spectrum and modulate the biodistribution, which can

minimize the background signals in PAT. Another type of modification is the use of polymers in the formation of J-aggregates, which can improve the PA signal generation.[189] Other dyes have been formulated with Pluronic micelles surfactant stripping, which results in concentrated dye suspensions for strong PA signal generation. For example, these micelles were used for PAT of mouse gut following oral administration, as shown in Figure 13.[190]

Genetic reporters. Genetically-encoded probes are usually developed for fluorescence imaging, but have become increasingly attractive in PAT as biomarkers of tumors or healthy cells.[191] With directed evolution, these probes can be modified for higher photostability, larger absorption coefficient in the NIR region, and more distinct spectra.[192,193] Genetically-encoded probes have good biocompatibility with much reduced toxicity concerns. However, wavelength tunability and manipulation of the absorption bandwidth is challenging. They often have relatively low concentration in cells and high photobleaching rate. Some genetic reporters can absorb strongly in the NIR-I region, but few if any have been developed with NIR-II absorption.[194]

One recent study reported PAT with red fluorescent protein (RFP) activated in the presence of biliverdin, which is typically found in the liver and spleen. It was evident this cofactor could also be directly injected into the tumor for localized PA signal
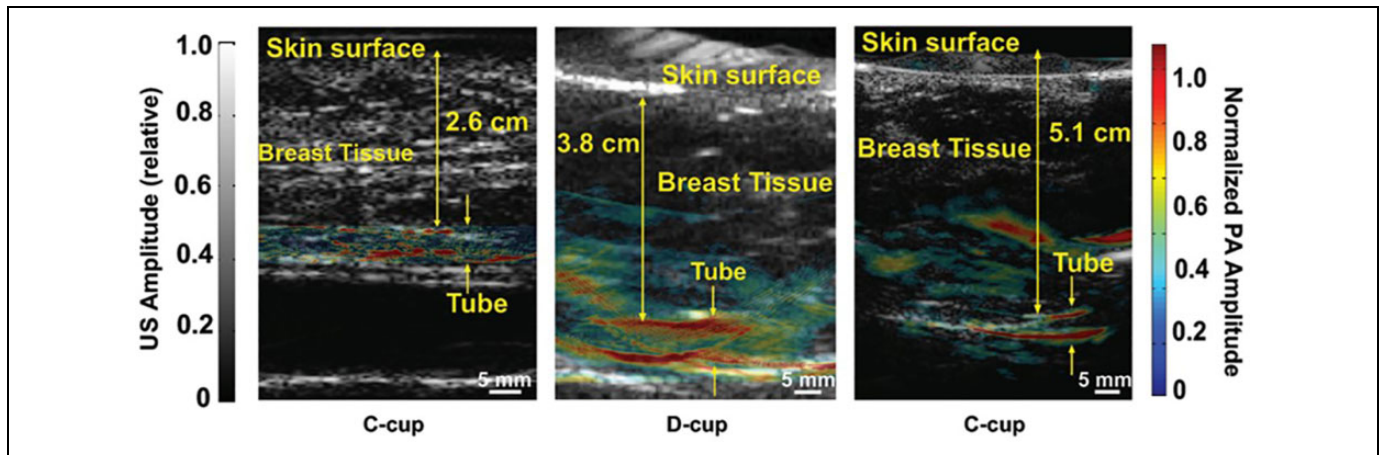
Figure 12. PA and US overlaid images of tube containing ss-CyFaP placed beneath the breasts of 3 different human adult female volunteers with indicated cup sizes. Reproduced with permission from.[184]

enhancement.[195] A similar concept has been developed that uses a viral delivery system with cell receptor tyrosine that triggers the human cancer cells to permanently express eumelanin. Using eumelanin as the endogenous contrast in the NIR-I region, PAT can be used to image tumor growth over time, as shown in Figure 14.[17]

One major hurdle in PAT of genetically encoded probes is the overwhelming background signals from the abundant hemoglobin. Recently, bacteriophytochromes (BphPs) have been reported as promising contrast for molecular PAT that can drastically improve the detection sensitivity. BphPs can be reversibly photoswitched between the Pfr (ON) and Pr (OFF) states, which is induced by the photoisomerization of biliverdin IX located inside the chromophore-binding pocket. The molar extinction coefficient of BphPs in the Pfr state at 780 nm is $\sim$70-folds higher that of oxy-hemoglobin. By repeatedly switching the BphPs between the ON and OFF states, the PA signals from the BphPs can be reliably extracted from the non-switching background hemoglobin signals.[196-200] Different photo-switchable probes can also be identified by using a machine-learning-based unmixing method.[197]

Activatable probe. To improve the detection specificity, a useful strategy in PA molecular imaging is the ability to activate a molecular probe under certain biological and physiological conditions. For example, Ju et al have demonstrated a nanoparticle formulation with a melanin core, whose PA signal can be amplified by 8 times in mildly acid conditions.[201] This nanoparticle is useful for cancer imaging due to the lower pH microenvironment inside a tumor. Wang et al have reported a new NIR probe 1-RGD that was activated by caspase-3, one of the chain events in apoptosis. Activation of 1-RGD lead to mono-dispersed nanoparticles with strong PA signal generation, which allowed for imaging tumor cell apoptosis.[202] Similarly, using plasmonic nanosensors activatable by epidermal growth
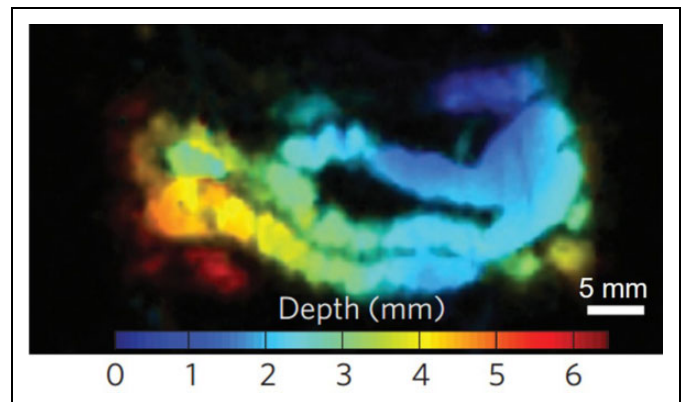

Figure 13. PAT of the mouse intestine after oral administration of frozen micelles of naphthalocyanine dye. The depth was encoded in color. Reproduced with permission from.[190]

factor receptor, Luke et al was able to image metastatic cancer cells.[22]

Another type of activatable PA probes can be used to record physiological signals. For example, Zhang et al have developed a voltage-sensitive probe that responds to the voltage stimulation via fluorescence quenching. This probe has the potential to record action potentials in the brain using PAT.[203] Similarly, another synthesized PA probe can be activated by Ca^{+2} and was able to measure electric potentials in the heart, brain, and skeletal muscles.[204]

Conclusion and Outlook

PAT has been demonstrated as a powerful technology to provide reliable molecular imaging. Various approaches have been explored to further improve PAT's penetration depth for molecular applications. Using microwave or X-ray as the radiation source can greatly increase the penetration depth, but the clinical application is limited to certain targets. NIR light can be
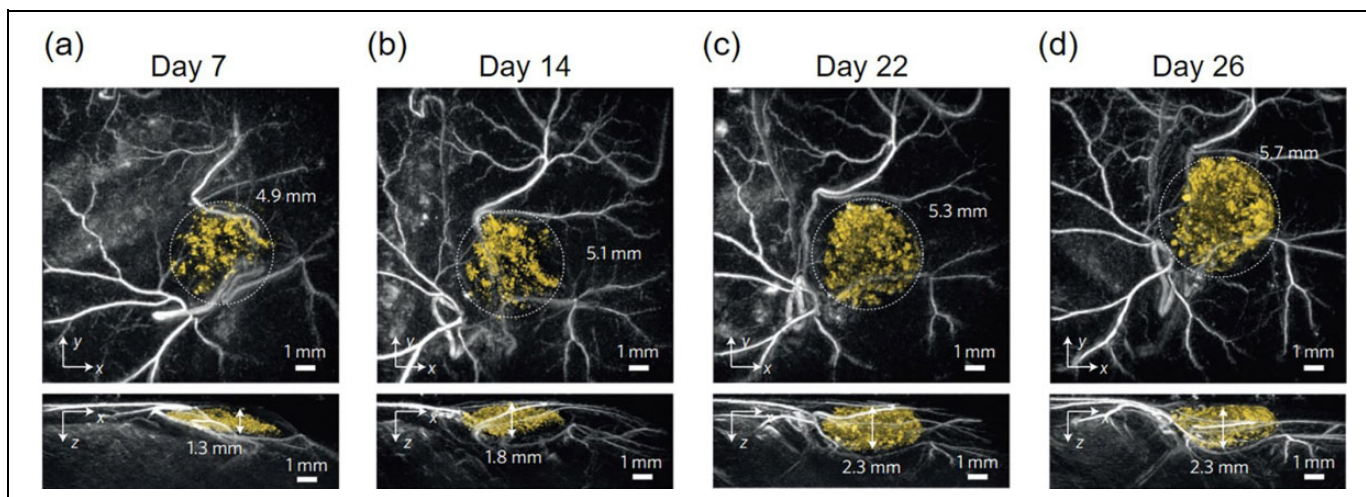
Figure 14. *In vivo* PAT of Tyr-expressing 293T cells acquired at different times post-inoculation, illustrating cell population growth. (a-d) Maximum amplitude projections of 3D image acquired on day 7 (a), day 14 (b), day 22 (c) and day 26 post-inoculation (d). Reproduced with permission from.[17]

applied in internal-illumination PAT or PA endoscopy to image organs closely located to body cavities. Wavefront shaping combined with ultrasensitive ultrasound transducers can further extend penetration depth. In addition, fluence compensation and artifact reduction reconstruction algorithms are actively applied to enhance PA images with weak signals. Deep-learning-based reconstruction methods are growing rapidly and have shown great promise to further improve the image quality at depths. Moreover, many types of novel molecular probes have been extensively studied as PAT contrast, and their strong optical absorption in the NIR region have resulted in improved penetration depth.

Future work in PA molecular imaging will likely include all of the above endeavors in a more integrated, rational, and clinically-oriented manner. For instance, internal-illumination PAT can be combined with advanced image reconstruction methods and high-absorbing molecular probes to future improve the SNR and image quality. Moreover, while many promising PA contrast agents have been developed, most of these studies were carried out in small animal models. There is a strong need to test these imaging paradigms in large animals. The costs for required sterile manufacturing and toxicity testing are substantially higher than the small animal applications, so rational selection of target indication is important. The clinical translation of PA molecular imaging is still progressing slowly but the potential impact is not beyond reach. For example, by using the FDA-approved indocyanine green, it is possible to apply PAT for detecting tumor malignancy during surgery.[205] Another solution is the repurposing of natural materials for PA molecular imaging. For example, roasted barley was found to have strong NIR-II PA signal and can be used to monitor swallowing in humans.[206] These natural materials have the potential to be used for human imaging and can be readily translated with minimized safety risk.

ORCID iD

Junjie Yao ⓘ https://orcid.org/0000-0002-2381-706X

References

1. James ML, Gambhir SS. A molecular imaging primer: modalities, imaging agents, and applications. *Physiol Rev*. 2012;92(2): 897–965.
2. Massoud TF, Gambhir SS. Molecular imaging in living subjects: seeing fundamental biological processes in a new light. *Genes Dev*. 2003;17(5):545–580.
3. Weissleder R. Molecular imaging in cancer. *Science*. 2006; 312(5777):1168–1171.
4. Weissleder R, Mahmood U. Molecular imaging. *Radiology*. 2001; 219(2):316–333.
5. Kenny LM, Aboagye EO, Price PM. Positron emission tomography imaging of cell proliferation in oncology. *Clin Oncol (R Coll Radiol)*. 2004;16(3):176–185.

6. Kennel SJ, Davis IA, Branning J, Pan H, Kabalka GW, Paulus MJ. High resolution computed tomography and MRI for monitoring lung tumor growth in mice undergoing radioimmunotherapy: correlation with histology. *Med Phys*. 2000;27(5):1101–1107.

7. Mallo RD, Salem L, Lalani T, Flum DR. Computed tomography diagnosis of ischemia and complete obstruction in small bowel obstruction: a systematic review. *J Gastrointest Surg*. 2005;9(5): 690–694.

8. Ribi W, Sendenb TJ, Sakellarioub A, Limayec A, Zhangd S. Imaging honey bee brain anatomy with micro-X-ray-computed tomography. *J Neurosci Methods*. 2008;171(1):93–97.

9. Sosnovik DE, Nahrendorf M, Panizzi P, et al. Molecular MRI detects low levels of cardiomyocyte apoptosis in a transgenic model of chronic heart failure. *Circ Cardiovasc Imaging*. 2009; 2(6):468–475.

10. Sun C, Veiseh O, Gunn J, et al. In vivo MRI detection of gliomas by chlorotoxin-conjugated superparamagnetic nanoprobes. *Small*. 2008;4(3):372–379.

11. Behm CZ, Lindner JR. Cellular and molecular imaging with targeted contrast ultrasound. *Ultrasound Q*. 2006;22(1):67–72.

12. Deshpande N, Needles A, Willmann JK. Molecular ultrasound imaging: current status and future directions. *Clin Radiol*. 2010; 65(7):567–581.

13. Foster FS, Hossack J, Adamson SL. Micro-ultrasound for preclinical imaging. *Interface Focus*. 2011;1(4):576–601.

14. Cheng Z, Levi J, Xiong Z, et al. Near-infrared fluorescent deoxyglucose analogue for tumor optical imaging in cell culture and living mice. *Bioconjug Chem*. 2006;17(3):662–669.

15. Couillard-Despres S, Finkl R, Winner B, et al. In vivo optical imaging of neurogenesis: watching new neurons in the intact brain. *Mol Imaging*. 2008;7(1):28–34.

16. Wang LV, Yao J. A practical guide to photoacoustic tomography in the life sciences. *Nat Methods*. 2016;13(8):627–638.

17. Jathoul AP, Laufer J, Ogunlade O, et al. Deep in vivo photoacoustic imaging of mammalian tissues using a tyrosinase-based genetic reporter. *Nat Photonics*. 2015;9(4):239–246.

18. Weber J, Beard PC, Bohndiek SE. Contrast agents for molecular photoacoustic imaging. *Nat Methods*. 2016;13(8):639–650.

19. Beard P. Biomedical photoacoustic imaging. *Interface Focus*. 2011;1(4):602–631.

20. Wang LV. Multiscale photoacoustic microscopy and computed tomography. *Nat Photonics*. 2009;3(9):503–509.

21. Wang LV, Hu S. Photoacoustic tomography: in vivo imaging from organelles to organs. *Science*. 2012;335(6075):1458–1462.

22. Luke GP, Myers JN, Emelianov SY, Sokolov KV. Sentinel lymph node biopsy revisited: ultrasound-guided photoacoustic detection of micrometastases using molecularly targeted plasmonic nanosensors. *Cancer Res*. 2014;74(19):5397–5408.

23. Nie L, Chen X, Structural and functional photoacoustic molecular tomography aided by emerging contrast agents. *Chem Soc Rev*. 2014;43(20):7132–7170.

24. Yao J, Wang LV. Recent progress in photoacoustic molecular imaging. *Curr Opin Chem Biol*. 2018;45:104–112.

25. Li M, Tang Y, Yao J.Photoacoustic tomography of blood oxygenation: a mini review. *Photoacoustics*. 2018;10:65–73.

26. Xia J, Yao J, Wang LV. Photoacoustic tomography: principles and advances. *Electromagn Waves (Camb)*. 2014;147:1–22.

27. Wu D, Huang L, Jiang MS, Jiang H. Contrast agents for photoacoustic and thermoacoustic imaging: a review. *Int J Mol Sci*. 2014;15(12):23616–23639.

28. Strohm EM, Moore MJ, Kolios MC. Single cell photoacoustic microscopy: a review. *IEEE J Sel Top*. 2016;22(3):137–151.

29. Ntziachristos V, Razansky D. Optical and opto-acoustic imaging. In: *Molecular Imaging in Oncology*. Springer; 2013:133–150.

30. Ntziachristos V. Going deeper than microscopy: the optical imaging frontier in biology. *Nat Methods*. 2010;7(8):603.

31. Xing W, Wang L, Maslov K, Wang LV. Integrated optical- and acoustic-resolution photoacoustic microscopy based on an optical fiber bundle. *Opt Lett*. 2013;38(1):52–54.

32. Moothanchery M, Pramanik M. Performance characterization of a switchable acoustic resolution and optical resolution photoacoustic microscopy system. *Sensors (Basel)*. 2017;17(2):357.

33. Dean-Ben XL, Fehm TF, Ford SJ, Gottschalk S, Razansky D. Spiral volumetric optoacoustic tomography visualizes multiscale dynamics in mice. *Light Sci Appl*. 2017;6(4):e16247.

34. Filonov GS, Krumholz A, Xia J, et al. Deep-tissue photoacoustic tomography of a genetically encoded near-infrared fluorescent probe. *Angewandte Chemie International Edition*. 2012;51(6): 1448–1451.

35. Yao J, Xiaa J, Maslov KI, et al. Noninvasive photoacoustic computed tomography of mouse brain metabolism in vivo. *Neuroimage*. 2013;64:257–266.

36. Li M, Liu C, Gong X, et al. Linear array-based real-time photoacoustic imaging system with a compact coaxial excitation handheld probe for noninvasive sentinel lymph node mapping. *Biomed Opt Exp*. 2018;9(4):1408–1422.

37. Li M, Lan B, Sankin G, et al. Simultaneous photoacoustic imaging and cavitation mapping in shockwave lithotripsy. *IEEE Trans Med Imaging*. 2020;39(2):468–477.

38. Cai X, Zhang Y, Li L, et al. Investigation of neovascularization in three-dimensional porous scaffolds in vivo by a combination of multiscale photoacoustic microscopy and optical coherence tomography. *Tissue Eng Part C: Methods*. 2012;19(3):196–204.

39. Yao J, Wang LV. Sensitivity of photoacoustic microscopy. *Photoacoustics*. 2014;2(2):87–101.

40. Vu T, Li M, Humayun H, Zhou Y, Yao J. A generative adversarial network for artifact removal in photoacoustic computed tomography with a linear-array transducer. *Exp Biol Med (Maywood)*. 2020;245(7):597–605.

41. Xu Y, Wang LV, Ambartsoumian G, Kuchment P. Reconstructions in limited-view thermoacoustic tomography. *Med Phys*. 2004;31(4):724–733.

42. Paltauf G, Nuster R, Burgholzer P. Weight factors for limited angle photoacoustic tomography. *Phys Med Biol*. 2009;54(11): 3303–3314.

43. Cao M, Feng T, Yuan J, Xu G, Wang X, Carson PL. Spread spectrum photoacoustic tomography with image optimization. *IEEE Trans Biomed Circuits Syst*. 2017;11(2):411–419.

44. Jeon M, Kim J, Kim C. Multiplane spectroscopic whole-body photoacoustic imaging of small animals in vivo. *Med Biol Eng Comput*. 2016;54(2-3):283–294.

45. Kellnberger S, Hajiaboli A, Razansky D, Ntziachristos V. Near-field thermoacoustic tomography of small animals. *Phys Med Biol*. 2011;56(11):3433–3444.

46. Kruger RA, Kopecky KK, Aisen AM, Reinecke DR, Kruger GA, Kiser, Jr WL. Thermoacoustic CT with radio waves: a medical imaging paradigm. *Radiology*. 1999;211(1):275–278.

47. Ai M, Youn J, Salcudean SE, Rohling R, Abolmaesumi P, Tang S. Photoacoustic tomography for imaging the prostate: a transurethral illumination probe design and application. *Biomed Opt Exp*. 2019;10(5):2588–2605.

48. Bungart B, Cao Y, Yang-Tran T, et al. Cylindrical illumination with angular coupling for whole-prostate photoacoustic tomography. *Biomed Opt Exp*. 2019;10(3):1405–1419.

49. Lediju Bell MA, Guo X, Song DY, Boctor EM. Transurethral light delivery for prostate photoacoustic imaging. *J Biomed Opt*. 2015;20(3):036002.

50. Li M, Liang S, Zhang J. Internal-illumination photoacoustic computed tomography. *J Biomed Opt*. 2018;23(3):1–4.

51. Ansari R, Zhang EZ, Desjardins AE, Beard PC. All-optical forward-viewing photoacoustic probe for high-resolution 3D endoscopy. *Light Sci Appl*. 2018;7:75.

52. Li H, Dong B, Zhang Z, Zhang HF, Sun C. A transparent broadband ultrasonic detector based on an optical micro-ring resonator for photoacoustic microscopy. *Sci Rep*. 2014;4:4496.

53. Rosenthal A, Razansky D, Ntziachristos V. High-sensitivity compact ultrasonic detector based on a pi-phase-shifted fiber Bragg grating. *Opt Lett*. 2011;36(10):1833–1835.

54. Engholm M, Bouzari H, Christiansen TL, et al. Probe development of CMUT and PZT row–column-addressed 2-D arrays. *Sens Actuators A: Phys*. 2018;273:121–133.

55. Qiu Y, Gigliotti JV, Wallace M, et al. Piezoelectric micromachined ultrasound transducer (PMUT) arrays for integrated sensing, actuation and imaging. *Sens (Basel)*. 2015;15(4):8020–8041.

56. Dean-Ben XL, Ford SJ, Razansky D. High-frame rate four dimensional optoacoustic tomography enables visualization of cardiovascular dynamics and mouse heart perfusion (vol 5, 10133, 2015). *Sci Rep*. 2015;5.

57. Ozbek A, Dean-Ben XL, Razansky D. Optoacoustic imaging at kilohertz volumetric frame rates. *Optica*. 2018;5(7):857–863.

58. Ozbekxs A, Dean-Ben XL, Razansky D. Compressed optoacoustic sensing of volumetric cardiac motion. *IEEE Trans Med Imaging*. 2020;39(10):3250–3255.

59. Davoudi N, Deán-Ben XL, Razansky D. Deep learning optoacoustic tomography with sparse data. *Nat Mach Intell*. 2019;1(10):453–460.

60. Ding L, Dean-Ben XL, Razansky D. Efficient 3-D model-based reconstruction scheme for arbitrary optoacoustic acquisition geometries. *IEEE Trans Med Imaging*. 2017;36(9):1858–1867.

61. Ding L, Razansky D, Dean-Ben XL. Model-based reconstruction of large three-dimensional optoacoustic datasets. *IEEE Trans Med Imaging*. 2020;39(9):2931–2940.

62. Zhang H, Li H, Nyayapathi N, et al. A New deep learning network for mitigating limited-view and under-sampling artifacts in ring-shaped photoacoustic tomography. *Comput Med Imaging Graph*. 2020;84:101720.

63. Guan S, Khan AA, Sikdar S, Chitnis PV. Limited-view and sparse photoacoustic tomography for neuroimaging with deep learning. *Sci Rep*. 2020;10(1):8510.

64. Peters VG, Wyman DR, Patterson MS, Frank GL. Optical properties of normal and diseased human breast tissues in the visible and near infrared. *Phys Med Biol*. 1990;35(9):1317–1334.

65. Jacques SL. Optical properties of biological tissues: a review. *Phys Med Biol*. 2013;58(11):R37–61.

66. Jeon S, Song HB, Kim J, et al. In Vivo photoacoustic imaging of anterior ocular vasculature: a random sample consensus approach. *Sci Rep*. 2017;7(1):4318.

67. Ku G, Wang LV. Deeply penetrating photoacoustic tomography in biological tissues enhanced with an optical contrast agent. *Opt Lett*. 2005;30(5):507–509.

68. Hoelen CG, de Mul FFM, Pongers R, Dekker A. Three-dimensional photoacoustic imaging of blood vessels in tissue. *Opt Lett*. 1998;23(8):648–650.

69. Menke J. Photoacoustic breast tomography prototypes with reported human applications. *Eur Radiol*. 2015;25(8):2205–2213.

70. Upputuri PK, Pramanik M. Pulsed laser diode based optoacoustic imaging of biological tissues. *Biomed Phys Eng Exp*. 2015;1(4):045010.

71. Kruger RA, Lam RB, Reinecke DR, Del Rio SP, Doyle RP. Photoacoustic angiography of the breast. *Med Phys*. 2010;37(11):6096–6100.

72. Zhou Y, Wang D, Zhang Y, et al. A Phosphorus phthalocyanine formulation with intense absorbance at 1000 nm for deep optical imaging. *Theranostics*. 2016;6(5):688–697.

73. Cui Y, Yuan C, Ji Z. A review of microwave-induced thermoacoustic imaging: excitation source, data acquisition system and biomedical applications. *J Innov Opt Heal Sci*. 2017;10(04):1730007.

74. Wang LV, Zhao X, Sun H, Ku G. Microwave-induced acoustic imaging of biological tissues. *Rev Sci Instrum*. 1999;70(9):3744–3748.

75. Razansky D, Kellnberger S, Ntziachristos V. Near-field radiofrequency thermoacoustic tomography with impulse excitation. *Med Phys*. 2010;37(9):4602–4607.

76. Kruger RA, Miller KD, Reynolds HE, Kiser WL Jr, Reinecke DR, Kruger GA. Breast cancer in vivo: contrast enhancement with thermoacoustic CT at 434 MHz-feasibility study. *Radiology*. 2000;216(1):279–283.

77. Pramanik M, Ku G, Li C, Wang LV. Design and evaluation of a novel breast cancer detection system combining both thermoacoustic (TA) and photoacoustic (PA) tomography. *Med Phys*. 2008;35(6):2218–2223.

78. Cao C, Nie L, Lou C, Xing D. The feasibility of using microwave-induced thermoacoustic tomography for detection and evaluation of renal calculi. *Phys Med Biol*. 2010;55(17):5203–5212.

79. Lin H, Weizhi Q, Jinyu X, et al. Thermoacoustic tomography: a novel method for early breast tumor detection. *X-Acoustics: Imaging and Sens*. 2015;1(1).

80. Pramanik M, Ku G, Li C, et al. Novel breast cancer detection system combining both thermoacoustic (TA) and photoacoustic (PA) tomography using carbon nanotubes (CNTs) as a dual

contrast agent. *Proceedings of SPIE—The International Society for Optical Engineering*. 2009;7177:71772G.

81. Ku G, Wang LV. Scanning thermoacoustic tomography in biological tissue. *Med Phys*. 2000;27(5):1195–1202.

82. Kruger RA, Kiser WL Jr, Miller KD, et al. Thermoacoustic CT: imaging principles. *Biomed Opt*. 2000;3916:150–159.

83. Ye F, Ji Z, Ding W, Lou C, Yang S, Xing D. Ultrashort microwave-pumped real-time thermoacoustic breast tumor imaging system. *IEEE Trans Med Imaging*. 2016;35(3):839–844.

84. Bohris C, Bayer T, Gumpinger R. Ultrasound monitoring of kidney stone extracorporeal shockwave lithotripsy with an external transducer: does fatty tissue cause image distortions that affect stone comminution? *J Endourol*. 2010;24(1):81–88.

85. Lin L, Xia J, Wong TTW, Li L, Wang LV. In vivo deep brain imaging of rats using oral-cavity illuminated photoacoustic computed tomography. *J Biomed Opt*. 2015;20(1):016019.

86. Lediju Bell MA, Kuo NP, Song DY, Kang JU, Boctor EM. In vivo visualization of prostate brachytherapy seeds with photoacoustic imaging. *J Biomed Opt*. 2014;19(12):126011.

87. Mitcham T, Dextrazeac K, Taghavia H, Melanconbc M, Bouchard R. Photoacoustic imaging driven by an interstitial irradiation source. *Photoacoustics*. 2015;3(2):45–54.

88. Kosoglu MA, Hood RL, Rossmeisl JH Jr, et al. Fiberoptic microneedles: novel optical diffusers for interstitial delivery of therapeutic light. *Lasers Surg Med*. 2011;43(9):914–920.

89. Mizeret JC, van den Bergh HE. Cylindrical fiberoptic light diffuser for medical applications. *Lasers Surg Med*. 1996;19(2):159–167.

90. Hasselgren L, Galt S, Hard S. Diffusive optical fiber ends for photodynamic therapy: manufacture and analysis. *Appl Opt*. 1990;29(30):4481–4488.

91. Vesselov L, Whittington W, Lilge L. Design and performance of thin cylindrical diffusers created in Ge-doped multimode optical fibers. *Appl Opt*. 2005;44(14):2754–2758.

92. Li M, Yao J. Internal-Illumination photoacoustic tomography enhanced by a graded-scattering fiber diffuser. *IEEE Trans Med Imaging*. 2020. Doi: 10.1109/TMI.2020.3027199.

93. Poletti ME, Goncalves D, Mazzaro I. X-ray scattering from human breast tissues and breast-equivalent materials. *Phys Med Biol*. 2002;47(1):47–63.

94. Xiang L, Han B, Carpenter C, Pratx G, Kuang Y, Xing L. X-ray acoustic computed tomography with pulsed x-ray beam from a medical linear accelerator. *Med Phys*. 2013;40(1):010701.

95. Kim J, Park E-Y, Jung Y, et al. X-Ray acoustic-based dosimetry using a focused ultrasound transducer and a medical linear accelerator. *IEEE Trans Radiat Plasma Med Sci*. 2017;1(6):534–540.

96. Hickling S, Lei H, Hobson M, Léger P, Wang X, El Naqa I. Experimental evaluation of x-ray acoustic computed tomography for radiotherapy dosimetry applications. *Med Phys*. 2017;44(2):608–617.

97. Hickling S, Hobson M, El Naqa I. Characterization of X-ray acoustic computed tomography for applications in radiotherapy dosimetry. *IEEE Trans Radiat Plasma Med Sci*. 2018;2(4):337–344.

98. Lee D, Park E-Y, Choi S, et al. GPU-accelerated 3D volumetric X-ray-induced acoustic computed tomography. *Biomed Opt Exp*. 2020;11(2):752–761.

99. Xiang L, Tang S, Ahmad M, Xing L. High resolution X-ray-induced acoustic tomography. *Sci Rep*. 2016;6:26118.

100. Ng AK, Abramson JS, Digumarthy SR, Reingold JS, Stone JR. Case records of the Massachusetts General Hospital. Case 24-2010. A 56-year-old woman with a history of Hodgkin's lymphoma and sudden onset of dyspnea and shock. *N Engl J Med*. 2010;363(7):664–675.

101. Chaigne T, Katz O, Boccara AC, Fink M, Bossy E, Gigan S. Controlling light in scattering media non-invasively using the photoacoustic transmission matrix. *Nature Photonics*. 2013;8(1):58–64.

102. Lai P, Wang L, Tay JW, Wang LV. Photoacoustically guided wavefront shaping for enhanced optical focusing in scattering media. *Nat Photonics*. 2015;9(2):126–132.

103. Tzang O, Piestun R. Lock-in detection of photoacoustic feedback signal for focusing through scattering media using wavefront shaping. *Opt Express*. 2016;24(24):28122–28130.

104. Ruan H, Liu Y, Xu J, Huang Y, Yang C. Fluorescence imaging through dynamic scattering media with speckle-encoded ultrasound-modulated light correlation. *Nature Photonics*. 2020;14:511–516.

105. Yaqoob Z, Psaltis D, Feld MS, Yang C. Optical phase conjugation for turbidity suppression in biological samples. *Nat Photonics*. 2008;2(2):110–115.

106. Yu Z, Li H, Lai P. Wavefront shaping and its application to enhance photoacoustic imaging. *Appl Sci*. 2017;7(12):1320.

107. Horstmeyer R, Ruan H, Yang C. Guidestar-assisted wavefront-shaping methods for focusing light into biological tissue. *Nat Photonics*. 2015;9:563–571.

108. Ahn C, Hwang B, Nam K, Jin H, Woo T, Park J-H. Overcoming the penetration depth limit in optical microscopy: adaptive optics and wavefront shaping. *J Innov Opt Health Sci*. 2019;12(04):1930002.

109. Tao X, Azucena O, Fu M, Zuo Y, Chen DC, Kubby J. Adaptive optics microscopy with direct wavefront sensing using fluorescent protein guide stars. *Opt Lett*. 2011;36(17):3389–3391.

110. Vellekoop IM, Aegerter CM. Scattered light fluorescence microscopy: imaging through turbid layers. *Opt Lett*. 2010;35(8):1245–1247.

111. Hsieh C-L, Pu Y, Grange R, Laporte G, Psaltis D. Imaging through turbid layers by scanning the phase conjugated second harmonic radiation from a nanoparticle. *Opt Express*. 2010;18(20).

112. Tay JW, Lai P, Suzuki Y, Wang LV. Ultrasonically encoded wavefront shaping for focusing into random media. *Sci Rep*. 2014;4:3918.

113. Liu Y, Lai P, Ma C, Xu X, Grabar AA, Wang LV. Optical focusing deep inside dynamic scattering media with near-infrared time-reversed ultrasonically encoded (TRUE) light. *Nat Commun*. 2015;6:5904.

114. Kong F, Silverman RH, Liu L, Chitnis PV, Lee KK, Chen YC. Photoacoustic-guided convergence of light through optically diffusive media. *Opt Lett*. 2011;36(11):2053–2055.

115. Vellekoop IM, Mosk AP. Focusing coherent light through opaque strongly scattering media. *Opt Lett*. 2007;32(16).

116. Caravaca-Aguirre AM, Conkey DB, Dove JD, Ju H, Murray TW, Piestun R. High contrast three-dimensional photoacoustic imaging through scattering media by localized optical fluence enhancement. *Opt Express*. 2013;21(22):26671–26676.

117. Winkler AM, Maslov K, Wang LV. Noise-equivalent sensitivity of photoacoustics. *J Biomed Opt*. 2013;18(9):097003.

118. Zhang C, Maslov K, Wang LV. Subwavelength-resolution label-free photoacoustic microscopy of optical absorption in vivo. *Opt Lett*. 2010;35(19):3195–3197.

119. Jiang XJ, Liu M-W, Shi F-F, Wang W, Wu X-M, Chen J-Y. A microscale linear phased-array ultrasonic transducer based on PZT ceramics. *Sens (Basel)*. 2019;19(5).

120. Yang JM, Favazza C, Chen R, et al. Simultaneous functional photoacoustic and ultrasonic endoscopy of internal organs in vivo. *Nat Med*. 2012;18(8):1297–1302.

121. Yang JM, Maslov K, Yang H-C, Zhou Q, Shung KK, Wang LV. Photoacoustic endoscopy. *Opt Lett*. 2009;34(10):1591–1593.

122. Yoon TJ, Cho YS. Recent advances in photoacoustic endoscopy. *World J Gastrointest Endosc*. 2013;5(11):534–539.

123. Jansen K, van Soest G, van der Steen AF. Intravascular photoacoustic imaging: a new tool for vulnerable plaque identification. *Ultrasound Med Biol*. 2014;40(6):1037–1048.

124. Wang B, Su JL, Karpiouk AB, Sokolov KV, Smalling RW, Emelianov SY. Intravascular photoacoustic imaging. *IEEE J Quantum Electron*. 2010;16(3):588–599.

125. Wissmeyer G, Pleitez MA, Rosenthal A, Ntziachristos V. Looking at sound: optoacoustics with all-optical ultrasound detection. *Light Sci Appl*. 2018;7:53.

126. Dausch DE, Castellucci JB, Chou DR, von Ramm OT. Theory and operation of 2-D array piezoelectric micromachined ultrasound transducers. *IEEE Trans Ultrason Ferroelectr Freq Control*. 2008;55(11):2484–2492.

127. Peng J, Chao C, Tang H. Piezoelectric micromachined ultrasonic transducer based on dome-shaped piezoelectric single layer. *Microsys Technol*. 2010;16(10):1771–1775.

128. Kothapalli SR, Ma T-J, Vaithilingam S, Oralkan Ö, Khuri-Yakub BT, Gambhir SS. Deep tissue photoacoustic imaging using a miniaturized 2-D capacitive micromachined ultrasonic transducer array. *IEEE Trans Biomed Eng*. 2012;59(5):1199–1204.

129. Khuri-Yakub BT, Oralkan O. Capacitive micromachined ultrasonic transducers for medical imaging and therapy. *J Micromech Microeng*. 2011;21(5):54004–54014.

130. Vallet M, Varraya F, Boutet J, et al. Quantitative comparison of PZT and CMUT probes for photoacoustic imaging: experimental validation. *Photoacoustics*. 2017;8:48–58.

131. Wygant IO, Wygant IO, Zhuang X, Yeh DT, et al. Integration of 2D CMUT arrays with front-end electronics for volumetric ultrasound imaging. *IEEE Trans Ultrason Ferroelectr Freq Control*. 2008;55(2):327–342.

132. Guggenheim JA, Li J, Allen TJ, et al. Ultrasensitive plano-concave optical microresonators for ultrasound sensing. *Nat Photonics*. 2017;11(11):714–719.

133. Dong B, Sun C, Zhang HF. Optical detection of ultrasound in photoacoustic imaging. *IEEE Trans Biomed Eng*. 2017;64(1):4–15.

134. Dong B, Chen S, Zhang Z, Sun C, Zhang HF. Photoacoustic probe using a microring resonator ultrasonic sensor for endoscopic applications. *Opt Lett*. 2014;39(15):4372–4375.

135. Zhang EZ, Laufer JG, Pedley RB, Beard PC. In vivo high-resolution 3D photoacoustic imaging of superficial vascular anatomy. *Phys Med Biol*. 2009;54(4):1035–1046.

136. Zhang E, Laufer J, Beard P. Backward-mode multiwavelength photoacoustic scanner using a planar Fabry-Perot polymer film ultrasound sensor for high-resolution three-dimensional imaging of biological tissues. *Appl Opt*. 2008;47(4):561–577.

137. Chen SL, Xiea Z, Guob LJ, Wang X. A fiber-optic system for dual-modality photoacoustic microscopy and confocal fluorescence microscopy using miniature components. *Photoacoustics*. 2013;1(2):30–35.

138. Campanella CE, Cuccovillo A, Campanella C, Yurt A, Passaro VMN. Fibre Bragg grating based strain sensors: review of technology and applications. *Sensors (Basel)*. 2018;18(9).

139. Zhang EZ, Beard PC. A miniature all-optical photoacoustic imaging probe. *Proceedings of SPIE Photons Plus Ultrasound: Imaging and Sensing*. 2011;7899:78991F.

140. Liang Y, Jin L, Wang L, Bai X, Cheng L, Guan B-O. Fiber-laser-based ultrasound sensor for photoacoustic imaging. *Sci Rep*. 2017;7:40849.

141. Sivasubramanian K, Pramanik M. High frame rate photoacoustic imaging at 7000 frames per second using clinical ultrasound system. *Biomed Opt Exp*. 2016;7(2):312–323.

142. Zhu YH, Xu G, Yuan J, et al. Light emitting diodes based photoacoustic imaging and potential clinical applications. *Sci Rep*. 2018;8.

143. Sandbichler M, Krahmer F, Berer T, Burgholzer P, Haltmeier M. A novel compressed sensing scheme for photoacoustic tomography. *Siam J Appl Math*. 2015;75(6):2475–2494.

144. Xi L, Li X, Yao L, Grobmyer S, Jiang H. Design and evaluation of a hybrid photoacoustic tomography and diffuse optical tomography system for breast cancer detection. *Med Phys*. 2012;39(5):2584–2594.

145. Xu C, Kumavor PD, Alqasemi US, et al. Indocyanine green enhanced co-registered diffuse optical tomography and photoacoustic tomography. *J Biomed Opt*. 2013;18(12):126006.

146. Xu C, Kumavor PD, Aguirre A, Zhu Q. Investigation of a diffuse optical measurements-assisted quantitative photoacoustic tomographic method in reflection geometry. *J Biomed Opt*. 2012;17(6):061213.

147. Cox BT, Laufer JG, Beard PC, Arridge SR. Quantitative spectroscopic photoacoustic imaging: a review. *J Biomed Opt*. 2012;17(6):061202.

148. Hussain A, Hondebrink E, Staley J, Steenbergen W. Photoacoustic and acousto-optic tomography for quantitative and functional imaging. *Optica*. 2018;5(12).

149. Kim M, Jengb G-S, O'Donnella M, Pelivanov I. Correction of wavelength-dependent laser fluence in swept-beam spectroscopic photoacoustic imaging with a hand-held probe. *Photoacoustics*. 2020;19:100192.

150. Jin H, Zhang R, Liu S, Zheng Z, Zheng Y. A single sensor dual-modality photoacoustic fusion imaging for compensation of

light fluence variation. *IEEE Transact Biomed Eng*. 2019;66(6): 1810–1813.

151. Fadhel MN, Hysi E, Assi H, Kolios MC. Fluence-matching technique using photoacoustic radiofrequency spectra for improving estimates of oxygen saturation. *Photoacoustics*. 2020;19:100182.

152. Cox B, Laufer J, Beard P. The challenges for quantitative photoacoustic imaging. in photons plus ultrasound: imaging and sensing 2009. *Int Soc Optics Photonic*. 2009;7177(2009)..

153. Maslov K, Zhang HF, Wang LV. Effects of wavelength-dependent fluence attenuation on the noninvasive photoacoustic imaging of hemoglobin oxygen saturation in subcutaneous vasculature in vivo. *Inver Probl*. 2007;23(6):S113.

154. Tzoumas S, Nunes A, Olefir I, et al. Eigenspectra optoacoustic tomography achieves quantitative blood oxygenation imaging deep in tissues. *Nat Commun*. 2016;7:12121.

155. Olefir I, Tzoumas S, Yang H, Ntziachristos V. A Bayesian approach to Eigenspectra optoacoustic tomography. *IEEE Trans Med Imaging*. 2018;37(9):2070–2079.

156. Xu M, Wang LV. Universal back-projection algorithm for photoacoustic computed tomography. *Phys Rev E Stat Nonlin Soft Matter Phys*. 2005;71(1 pt 2):16706.

157. Arnal B, Perez C, Wei C-W, et al. Sono-photoacoustic imaging of gold nanoemulsions: part I. Exposure thresholds. *Photoacoustics*. 2015;3(1):3–10.

158. Prakash J, Mandal S, Razansky D, Ntziachristos V. Maximum entropy based non-negative optoacoustic tomographic image reconstruction. *IEEE Trans Biomed Eng*. 2019;66(9):2604–2616.

159. Fletcher R. *Practical Methods of Optimization*. John Wiley & Sons; 2013.

160. Han Y, Ding L, Ben XL, Razansky D, Prakash J, Ntziachristos V. Three-dimensional optoacoustic reconstruction using fast sparse representation. *Optics Lett*. 2017;42(5):979–982.

161. Ding L, Deán-Ben XL, Lutzweiler C, Razansky D, Ntziachristos V. Efficient non-negative constrained model-based inversion in optoacoustic tomography. *Phys Med Biol*. 2015;60(17):6733.

162. Mastanduno MA, Gambhir SS. Quantitative photoacoustic image reconstruction improves accuracy in deep tissue structures. *Biomed Opt Exp*. 2016;7(10):3811–3825.

163. Banerjee B, Bagchi S, Vasu RM, Roy D. Quantitative photoacoustic tomography from boundary pressure measurements: noniterative recovery of optical absorption coefficient from the reconstructed absorbed energy map. *J Optic Soc Am A*. 2008; 25(9):2347–2356.

164. Hauptmann A, Lucka F, Betcke M, et al. Model-based learning for accelerated, limited-view 3-d photoacoustic tomography. *IEEE Transact Med Imag*. 2018;37(6):1382–1393.

165. Antholzer S, Schwab J, Haltmeier M. Deep learning versus ℓ^{1}-Minimization for compressed sensing photoacoustic tomography. In: *IEEE International Ultrasonics Symposium (IUS)*. 2018. IEEE.

166. Schwab J, Antholzer S, Nuster R, Haltmeier M. *Real-Time Photoacoustic Projection imaging Using Deep Learning*. arXiv preprint arXiv:1801.06693; 2018.

167. Goodfellow I, Bengio Y, Courville A. *Deep Learning*. MIT Press; 2016.

168. Antholzer S, Haltmeier M, Schwab J. Deep learning for photoacoustic tomography from sparse data. *Inver Probl Sci Eng*. 2019;27(7):987–1005.

169. Allman D, Reiter A, Bell MAL. Photoacoustic source detection and reflection artifact removal enabled by deep learning. *IEEE Transact Med Imag*. 2018;37(6):1464–1477.

170. Schwab J, Antholzer S, Nuster R, Paltauf G, Haltmeier M. Deep learning of truncated singular values for limited view photoacoustic tomography. In: Oraevsky AA, Wang LV, eds. *Photons Plus Ultrasound: Imaging and Sensing 2019*. International Society for Optics and Photonics; 2019.

171. Bench C, Hauptmann A, Cox B. Towards accurate quantitative photoacoustic imaging: learning vascular blood oxygen saturation in 3D. arXiv preprint arXiv:2005. 01089.

172. Cai C, Deng K, Ma C, Luo J. End-to-end deep neural network for optical inversion in quantitative photoacoustic imaging. *Opt Lett*. 2018;43(12):2752–2755.

173. Chen T, Lu T, Song S, Miao S, Gao F, Li J. A deep learning method based on U-Net for quantitative photoacoustic imaging. In: Oraevsky AA, Wang LV, eds. *Photons Plus Ultrasound: Imaging and Sensing 2020*. 2020.

174. Kim J-W, Galanzha EI, Shashkov EV, Moon HM, Zharov VP. Golden carbon nanotubes as multimodal photoacoustic and photothermal high-contrast molecular agents. *Nat Nanotechnol*. 2009;4(10):688–694.

175. Wang C, Bao C, Liang S, et al. RGD-conjugated silica-coated gold nanorods on the surface of carbon nanotubes for targeted photoacoustic imaging of gastric cancer. *Nanoscale Res Lett*. 2014;9(1):264.

176. Wang H, Huff TB, Zweifel DA, et al. In vitro and in vivo two-photon luminescence imaging of single gold nanorods. *PNAS USA*. 2005;102(44):15752–15756.

177. Chen Y-S, Zhao Y, Yoon SJ, Gambhir SS, Emelianov S. Miniature gold nanorods for photoacoustic molecular imaging in the second near-infrared optical window. *Nat Nanotechnol*. 2019; 14(5):465–472.

178. Li C, Zhang Y, Wang M, et al. In vivo real-time visualization of tissue blood flow and angiogenesis using Ag2S quantum dots in the NIR-II window. *Biomaterials*. 2014;35(1):393–400.

179. Ong G, Robinson JT, Zhang Y, et al. In vivo fluorescence imaging with Ag2S quantum dots in the second near-infrared region. *Angew Chem Int Ed*. 2012;51(39):9818–9821.

180. Dong B, Li C, Chen G, et al. Facile synthesis of highly photoluminescent Ag2Se quantum dots as a new fluorescent probe in the second near-infrared window for in vivo imaging. *Chem Mater*. 2013;25(12):2503–2509.

181. He X, Wang K, Cheng Z. In vivo near-infrared fluorescence imaging of cancer with nanoparticle-based probes. *Wiley Interdiscip Rev Nanomed Nanobiotechnol*. 2010;2(4): 349–366.

182. He X, Gao J, Gambhir SS, Cheng Z. Near-infrared fluorescent nanoprobes for cancer molecular imaging: status and challenges. *Trends Mol Med*. 2010;16(12):574–583.

183. Janib SM, Moses AS, MacKay JA. Imaging and drug delivery using theranostic nanoparticles. *Adv Drug Deliv Rev*. 2010; 62(11):1052–1063.

184. Chitgupi U, Nyayapathi N, Kim J, et al. Surfactant-stripped micelles for NIR-II photoacoustic imaging through 12 cm of breast tissue and whole human breasts. *Adv Mater*. 2019; 31(40):1902279.

185. Li K, Liu B. Polymer-encapsulated organic nanoparticles for fluorescence and photoacoustic imaging. *Chem Soc Rev*. 2014; 43(18):6570–6597.

186. Wan H, Yue J, Zhu S, et al. A bright organic NIR-II nanofluorophore for three-dimensional imaging into biological tissues. *Nat Commun*. 2018;9(1):1171.

187. Wang Q, Xia B, Xu J, et al. Biocompatible small organic molecule phototheranostics for NIR-II fluorescence/photoacoustic imaging and simultaneous photodynamic/photothermal combination therapy. *Mater Chem Front*. 2019;3(4):650–655.

188. Antaris AL, Chen H, Cheng K, et al. A small-molecule dye for NIR-II imaging. *Nat Mater*. 2016;15(2):235–242.

189. Sun P, Wu Q, Sun X, et al. J-Aggregate squaraine nanoparticles with bright NIR-II fluorescence for imaging guided photothermal therapy. *Chem Comm*. 2018;54(95):13395–13398.

190. Zhang Y, Jeon M, Rich LJ, et al. Non-invasive multimodal functional imaging of the intestine with frozen micellar naphthalocyanines. *Nat Nanotechnol*. 2014;9(8):631–638.

191. Deliolanis NC, Ale A, Morscher S, et al. Deep-tissue reporter-gene imaging with fluorescence and optoacoustic tomography: a performance overview. *Mol Imaging Biol*. 2014;16(5):652–660.

192. Razansky D, Distel M, Vinegoni C, et al. Multispectral optoacoustic tomography of deep-seated fluorescent proteins in vivo. *Nat Photonics*. 2009;3(7):412–417.

193. Shaner NC, Campbell RE, Steinbach PA, Giepmans BN, Palmer AE, Tsien RY. Improved monomeric red, orange and yellow fluorescent proteins derived from Discosoma sp. red fluorescent protein. *Nat Biotechnol*. 2004;22(12):1567–1572.

194. Laufer J, Jathoul A, Pule M, Beard P. In vitro characterization of genetically expressed absorbing proteins using photoacoustic spectroscopy. *Biomed Opt Express*. 2013;4(11):2477–2490.

195. Filonov GS, Krumholz A, Xia J, Yao J, Wang LV, Verkhusha VV. Deep-tissue photoacoustic tomography of a genetically encoded near-infrared fluorescent probe. *Angew Chem Int Ed Engl*. 2012;51(6):1448–1451.

196. Li L, Shemetov AA, Baloban M, et al. Small near-infrared photochromic protein for photoacoustic multi-contrast imaging and detection of protein interactions in vivo. *Nature Communicat*. 2018;9(1):1–4.

197. Mishra K, Stankevych M, Fuenzalida-Werner JP, et al. Multiplexed whole-animal imaging with reversibly switchable optoacoustic proteins. *Sci Adv*. 2020;6(24):eaaz6293.

198. Yao JJ, Kaberniuk AA, Li L, et al. Multiscale photoacoustic tomography using reversibly switchable bacterial phytochrome as a near-infrared photochromic probe. *Nature Methods*. 2016; 13(1):67–73.

199. Stiel AC, Deán-Ben XL, Jiang Y, Ntziachristos V, Razansky D, Westmeyer GG. High-contrast imaging of reversibly switchable fluorescent proteins via temporally unmixed multispectral optoacoustic tomography. *Opt Lett*. 2015;40(3): 367–370.

200. Märk J, Dortay H, Wagener A, et al. Dual-wavelength 3D photoacoustic imaging of mammalian cells using a photoswitchable phytochrome reporter protein. *Commun Phys*. 2018;1(1): 1–10.

201. Ju K-Y, Kang J, Pyo J, Lim J, Chang JH, Lee JK. pH-Induced aggregated melanin nanoparticles for photoacoustic signal amplification. *Nanoscale*. 2016;8(30):14448–14456.

202. Wang Y, Hu X, Weng J, et al. A photoacoustic probe for the imaging of tumor apoptosis by caspase-mediated macrocyclization and self-assembly. *Angew Chem Int Ed*. 2019;131(15): 4940–4944.

203. Zhang HK, Yan P, Kang J, et al. Listening to membrane potential: photoacoustic voltage-sensitive dye recording. *J Biomed Opt*. 2017;22(4):45006.

204. Roberts S, Seeger M, Jiang Y, et al. Calcium sensor for photoacoustic imaging. *J Am Chem Soc*. 2018;140(8):2718–2721.

205. Miyata A, Ishizawa T, Kamiya M, et al. Photoacoustic tomography of human hepatic malignancies using intraoperative indocyanine green fluorescence imaging. *PloS One*. 2014;9(11): e112667.

206. Wang D, Lee DH, Huang H, et al. Ingestible roasted barley for contrast-enhanced photoacoustic imaging in animal and human subjects. *Biomaterials*. 2018;175:72–81.